

Long-range waveguide-quantum electrodynamics with left-handed transmission lines

P. Goswami,¹ J. Liu,¹ C. A. González-Gutiérrez,^{2,3} and A. Kamal^{1,2,*}

¹*Department of Physics and Astronomy, Northwestern University, Evanston, IL 60208, USA*

²*Department of Physics and Applied Physics, University of Massachusetts, Lowell, MA 01854, USA*

³*Instituto de Ciencias Físicas, Universidad Nacional Autónoma de México, Cuernavaca 62210, Mexico*

(Dated: March 6, 2026)

While engineering long-range light-matter interactions is the principal aim in waveguide-QED, ironically most of the building blocks rest on local short-range couplings, such as nearest-neighbor-coupled cavity arrays employed in canonical models. Here, we propose a waveguide-QED system with native long-range interactions, comprising a single emitter coupled to a left-handed transmission line (LHTL). Interestingly, the LHTL emulates a synthetic photonic lattice with a slow logarithmic decay of hopping amplitudes over a distance set entirely by the ratio of UV and IR cutoffs of line dispersion. Its intrinsic long-range nature manifests both in the properties of atom-photon bound and scattering states, which exhibit algebraic localization and accelerated photon propagation respectively. Using a method of ‘running exponents’, we develop a unified picture connecting waveguide dispersion to bound state and light front profiles obtained in the strong long-range hopping regime. These results motivate how transmission lines can enable multi-qubit information processing with tunable-range interactions.

I. INTRODUCTION

Waveguide quantum electrodynamics has emerged as a new paradigm to explore cooperative effects in light-matter interactions and implement new quantum information functionalities based on itinerant photons, such as remote entanglement generation and quantum communication. Low dimensional waveguide-QED platforms, such as those based on superconducting qubits coupled to microwave waveguides (a.k.a transmission lines), are particularly appealing given their ease of control, high coupling efficiencies [1], as well as the significant design freedom afforded by such systems – all the way from tunable atoms with user-defined coupling modalities, to exotic waveguide geometries. A recent example is ‘giant’ atom waveguide-QED where a single qubit can be coupled at multiple points to a transmission line in order to engineer effects such as nonexponential atomic decay [2] and directional photon transmission [3]. It is worthwhile to note that almost all such variations and demonstrations till date are based on right-handed transmission lines (RHTLs), with the design focus being on the qubit or its coupling to the transmission line. Inspired by ideas from optical metamaterials, there has been increasing interest in exploring opportunities offered by engineering the transmission line or waveguide instead [4, 5] that can enable almost a ‘brass tacks’ approach to modifying the spectral properties of the photonic continuum. In this vein, one-dimensional left-handed transmission lines (LHTLs) present an intriguing alternative and a perfect dual to their conventional right-handed counterparts, with the roles of inductors and capacitors along the line interchanged. While such a change may seem superficially minimal at first glance, it constitutes a highly non-trivial modification of the line dispersion, as evidenced

by the new physical effects already reported in LHTL systems, namely particle production out of the quantum vacuum [6], generation of highly entangled states [7], and simulation of interesting quantum optical and thermodynamic effects in composite LH/RHTL systems [8].

Of particular importance in waveguide-QED are the entangled states known as atom-photon bound states, which are non-radiative states arising due to photonic band gaps. These states lead to long-lived, spatially-localized excitations due to vanishing group velocities near the band edge and can be leveraged to implement strong photonic or multi-emitter interactions. Recently there has been renewed interest in waveguide engineering, via periodic loading [9], staggered hoppings [10] or impedance engineering [11], to extend the range of localized bound-state wavefunction. Nonetheless, all these approaches focus almost exclusively on tweaking standard waveguide models based on coupled-cavity arrays with quadratic or cosine-like dispersion relations, and report an increase in the localization length while maintaining exponential bound-state profiles. In contrast, here we report how TL-based waveguide-QED systems exhibit functionally distinct algebraic localization, with a polynomial fall off with distance from the emitter. This is one of the central contributions of this paper and indicates how TL-based waveguide-QED provides a qualitatively new means to design long-range interactions in spin-boson and quantum impurity models.

Specifically, LHTL waveguide with its inverted dispersion maps to an unusual lattice hosting power-law hoppings with a distance-dependent exponent. This makes it a unique platform for emulating photonic lattices with strong long-range, weak long-range and short-range hoppings in the same system sampled at different length scales. Using this mapping as a backdrop, we establish direct connections between bound-state and scattering properties across these regimes, including appearance of algebraic localization and accelerated light cones due to

* archana.kamal@northwestern.edu

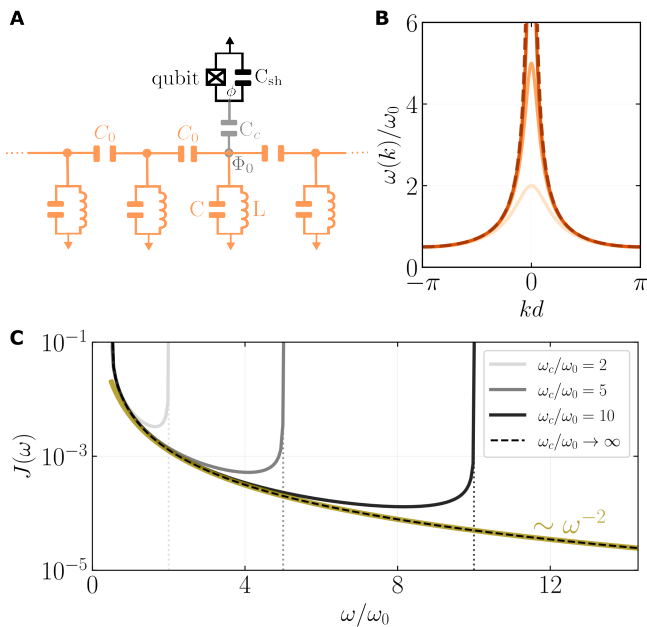


FIG. 1. **Left-handed waveguide-QED.** **A** Circuit representation for a transmon qubit capacitively coupled to a LHTL. **B** LHTL dispersion for different values of UV cutoff ω_c . **C** Spectral density seen by the qubit for the same set of cutoff frequencies.

strong long-range hoppings – a regime hitherto inaccessible to waveguide QED. Crucially, though perhaps unsurprisingly, this complexity also reflects in enhanced non-Markovianity in dynamics of the emitter coupled to an LHTL, with relaxation times that can even decrease with increase in emitter frequency in contrast to the behavior observed in the presence of usual Ohmic baths.

II. RESULTS

A. Left-handed transmission-line waveguide-QED platform

The left-handed waveguide-QED system we consider here consists of a two-level emitter coupled locally to a left-handed transmission line (LHTL); Fig.1A shows a superconducting circuit-based realization of such a system with the two-level emitter shown as a superconducting transmon qubit, coupled capacitively to an LHTL depicted using the equivalent telegrapher model for microwave transmission lines [6]. The LHTL dispersion relation is given by

$$\omega_k = \frac{\omega_0 \omega_c}{\sqrt{\omega_0^2 + 2\omega_c^2(1 - \cos(kd))}}, \quad (1)$$

where d denotes the inter unit-cell separation (set to unity in dimensionless units), $\omega_0 = (LC_0)^{-1/2}$. The left-handedness of the transmission line arises from the phase and group velocities being opposite in sign ($v_p v_g < 0$) as

evident from the dispersion plotted in Fig.1B. It is worth noting that we have included a capacitance to ground in the LHTL model presented here; besides being relevant to realistic experimental realizations, this also imposes a finite UV cutoff $\omega_c = (LC)^{-1/2}$ on the LHTL pass-band. For infinite UV-cutoff ($\omega_c \rightarrow \infty$), the dispersion reduces to the form $\omega_k = \omega_0/2|\sin(k/2)|$ with has a pole at $k = 0$. Introducing a finite capacitance to ground regularizes this divergence without affecting the handedness of the line.

Starting from the full circuit Lagrangian, we obtain the standard waveguide-QED Hamiltonian in the single-excitation regime under rotating-wave approximation (RWA),

$$H = \Delta \sigma^+ \sigma^- + \sum_{k=1}^N \omega_k a_k^\dagger a_k + \sum_{k=1}^N (g_k \sigma^+ a_k + \text{h.c.}), \quad (2)$$

where Δ is the emitter frequency, $\{g_k\}$ denote the momentum-dependent emitter-waveguide coupling constants, and N is the number of unit cells in the transmission line. Here k indexes the wave-vector number and associated operators defined in the momentum basis (see Supplementary Materials). The inverted dispersion of LHTL presents an unconventional spectral profile to the emitter, $J(\omega) = 2\pi \sum_k |g_k|^2 \delta(\omega - \omega_k)$,

$$J(\omega) = \frac{2g^2\omega_0^2}{\omega^3 \sqrt{1 - \left[1 - \frac{\omega_0^2}{2} \left(\frac{1}{\omega^2} - \frac{1}{\omega_c^2}\right)\right]^2}}, \quad (3a)$$

$$\approx \frac{2g^2\omega_0}{\omega^2}, \quad \text{for } \omega_0 \ll \omega \ll \omega_c. \quad (3b)$$

The behavior of the spectral function $J(\omega)$ with increasing UV cutoff (ω_c) is shown in Fig. 1C. It exhibits square-root van Hove singularities at the two band edges $\omega_{\text{IR}} = \omega_0 \omega_c / \sqrt{\omega_0^2 + 4\omega_c^2}$ and $\omega_{\text{UV}} = \omega_c$, though the UV and IR frequency cutoffs now appear at long ($k = 0$) and short ($k = \pi$) wavelengths, respectively, due to inverted LHTL dispersion. As shown in Eq. 3b, away from the band-edges, LHTL presents a Brownian spectrum $J(\omega) \sim 1/\omega^2$, making it natively non-Markovian. This is in sharp contrast to conventional right-handed systems and coupled cavity-arrays that almost always behave as Markovian environments due to their spectral function being flat away from the edges, and which typically rely on non-local emitter-waveguide couplings (giant-atom) or time-delay geometries to engineer non-Markovian effects. Further, even for non-Markovian noise, $J(\omega) \propto \omega^s$ with $s = -2$ is unusual from the perspective of spin-boson physics where studies on non-Ohmic spectra have been restricted to sub-Ohmic baths with $0 < s < 1$. While spin-boson models with inverted spectral densities ($s < 0$) have recently been explored in the context of spin dephasing [12], similar studies for finite-frequency processes such as spin relaxation have not been pursued to the best of our knowledge. Thus, transmission

line-based waveguide-QED systems provide an interesting and experimentally-viable alternative to explore exotic spin-boson models with tailored spectral densities.

Note that in Eq. 3, we have assumed a ‘flat’ $g_k \equiv g/\sqrt{N} \forall k$ for analytical tractability. In the following sections, we will continue to use this simple coupling profile to study both bound- and scattering-state properties, since that allows highlighting the salient features due to inverted LHTL dispersion alone. Later, we will include the full momentum dependence of emitter-waveguide coupling, though this would not significantly alter the qualitative features of the results obtained with g ; for instance, the emitter-photon bound state exhibits algebraic localization in both cases though the exponent is modified by the coupling profile g_k .

B. Beyond power-law hoppings

Starting with seminal work of Bak, Tang and Wiesenfeld [13], there have been several works which have provided tantalizing pointers on how spatially extended modes can lead to $1/\omega^s$ spectrum. Given the Brownian spectrum derived in the previous section, it is natural to expect that photonic correlations in LHTL-type systems must be long-range. To concretize this notion, we develop a photonic tight-binding lattice model for LHTL. To this end, LHTL Hamiltonian can be written in the Wannier basis, where the cosine Fourier coefficients of the dispersion ω_k act as photon hopping amplitudes between sites separated by n unit cells, [14]

$$H_{\text{LH}} = \sum_{m \in \mathbb{Z}} \sum_{n \in \mathbb{Z}} \xi_n a_{m+n}^\dagger a_m, \quad (4a)$$

$$\xi_n = \frac{1}{\pi} \int_0^\pi \omega(k) \cos(nk) dk = \xi_{-n} \in \mathbb{R}, \quad (n \in \mathbb{Z}). \quad (4b)$$

For large n , the hopping amplitude are described by a modified Bessel function of second kind,

$$\xi_n \simeq \frac{\omega_0}{\pi} K_0\left(\frac{n\omega_0}{\omega_c}\right) \simeq \frac{\omega_0}{\pi} K_0\left(\frac{n}{n_\star}\right), \quad n_\star \equiv \frac{\omega_{\text{UV}}}{2\omega_{\text{IR}}}. \quad (5)$$

The standard asymptotes of $K_0(z)$ give

$$\xi(z) \simeq \frac{\omega_0}{\pi} \begin{cases} -\ln\left(\frac{z}{2}\right) - \gamma_E, & z \ll 1 \quad (1 \ll n \ll n_\star), \\ \sqrt{\frac{\pi}{2}} \frac{e^{-z}}{\sqrt{z}}, & z \gg 1 \quad (n \gg n_\star). \end{cases} \quad (6)$$

where, $z \equiv n/n_\star$, and $\gamma_E \approx 0.577$ is the Euler’s constant. The hopping amplitude profile of the LHTL exhibits a crossover from logarithmic to exponential falloff around $z = 1$ ($n = n_\star$), at a length scale entirely determined by the ratio of UV and IR cutoff frequencies (Fig. 2A). This ‘ultra’ long-range nature of hoppings in LHTL is further validated by the fact that a nearest-neighbor, or even the next-nearest-neighbor, real-space truncation of hoppings fails to reproduce the correct dispersion relation

for LHTL (see Supplementary Materials). In contrast, the hopping amplitude profile for RHTL follows a power law, $\xi^{\text{RH}}(z) = (\omega_0^3/\pi\omega_c^2) z^{-2}$, with no crossover length scale. This is consistent with RHTL dispersion being gapless ($\omega_{\text{IR}}^{\text{RH}} = 0$), leading to $n_\star \rightarrow \infty$.

Running exponent method—Since the LHTL hopping amplitudes in Eq. 6 do not follow a simple power-law, in order to enable a direct comparison with standard long-range models with power-law interactions, we parameterize the spatial profile of hoppings with a *scale-dependent* or ‘running’ power-law exponent, $\xi(z) \sim 1/n^f(z)$. Any positive, monotonically decreasing function $\xi(z)$ can be parameterized using

(i) running local exponent

$$\alpha(z) \equiv -\frac{d \ln \xi(z)}{d \ln z}, \quad (7)$$

with monotonicity implying $\alpha(z) > 0$, and

(ii) running global exponent $\bar{\alpha}(z; z_0)$

$$\begin{aligned} \xi(z) &= \xi(z_0) \left(\frac{z}{z_0}\right)^{-\bar{\alpha}(z; z_0)}, \\ \bar{\alpha}(z; z_0) &= \frac{1}{\ln(z/z_0)} \int_{z_0}^z \frac{\alpha(z')}{z'} dz' \end{aligned} \quad (8)$$

The location $z_0 = 1/n_\star$ is the unit-cell adjacent to the location of the emitter.

Applying this construction to left- and right-handed transmission lines, with the hopping profiles $\xi^{\text{LH}}(z) = (\omega_0/\pi) K_0(z)$, and $\xi^{\text{RH}}(z) = (\omega_0^3/\pi\omega_c^2) z^{-2}$, we obtain,

$$\alpha^{\text{LH}}(z) = z \frac{K_1(z)}{K_0(z)}, \quad \bar{\alpha}^{\text{LH}}(z; z_0) = \frac{\ln[K_0(z_0)/K_0(z)]}{\ln(z/z_0)}, \quad (9a)$$

$$\alpha^{\text{RH}}(z) = \bar{\alpha}^{\text{RH}}(z, z_0) = 2. \quad (9b)$$

In the running-exponent language, the RHTL realizes a trivial, scale-invariant $1/z^2$ hopping network, whereas the LHTL exhibits genuine scale-dependent hopping amplitudes, see Fig. 2B. From Eq. 9a, we find a well-defined boundary at $z_1 \simeq 0.60$ where $\alpha(z_1) = 1$, which separates strong ($\alpha < 1$) and weak ($\alpha > 1$) long-range hopping. In 1D, $\alpha = 1$ coincides with the integrability threshold of power-law tails [15]. From Eq. 9a, we find well-defined boundaries at $z_1 \simeq 0.60$ and $z_2 \simeq 1.55$ where $\alpha(z_{1,2}) = 1, 2$, which separates strong ($\alpha < 1$) to weak ($1 < \alpha < 2$) long-range hopping regime, and weak long-range to short-range hopping regimes ($\alpha > 2$), respectively.

The appearance of n_\star as the relevant crossover scale underscores how LHTL waveguide-QED provides a crucial insight into relevant interaction scale for multimode systems. Past works have explored hybrid left/right-handed transmission lines in circuit-QED waveguide setups, and identified ω_{IR}^{-1} as the relevant interaction length scale by mapping the spin-boson model to an effective 1D Ising system [7]. However, as highlighted by LHTL hopping profiles, Eq. 5, the relevant length scale is n_\star which

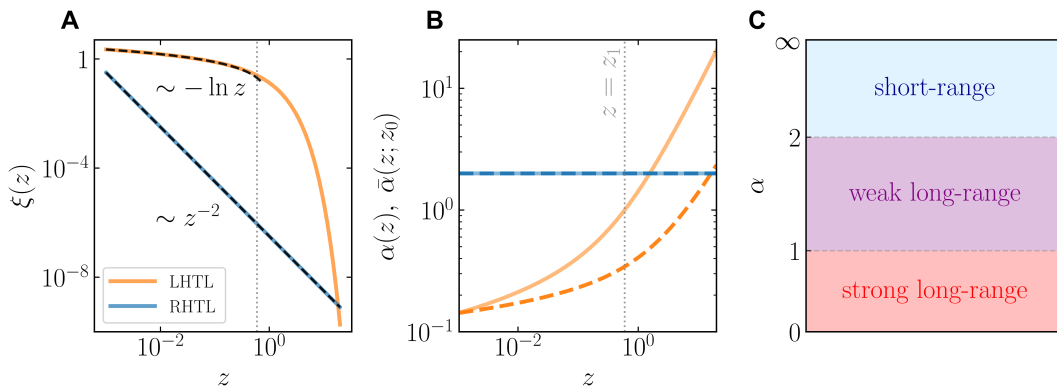


FIG. 2. **Hopping amplitudes for transmission lines.** **A** LHTL maps to a tight-binding photonic lattice with logarithmic fall off of hopping amplitudes $\xi(z)$ for $z < 1$, and exponential fall off for $z > 1$ ($z \equiv n/n_*$), while RHTL maps to a power-law hopping network with a constant exponent $\alpha = 2$. **B** Position-dependent local (solid) and global (dashed) hopping exponents for LHTL and RHTL obtained using the running exponent method. **C** Long-range regimes for 1D power-law hopping network, with $\alpha \rightarrow \infty$ corresponding to nearest-neighbor models.

is a ratio of UV and IR frequencies. Interestingly, this implies that interaction scale in LHTL-based waveguide networks can be pushed to infinity by pushing the waveguide UV cutoff ω_c higher even in the presence of a finite IR cutoff.

Here, we have used the running exponent method to identify the regime for strong vs weak-long range hopping [15]. We will use similar analysis later for developing a unified picture for explaining spatial profiles of bound states and temporal profiles of constant-intensity light fronts for scattering states, specifically establishing connections of both local bound state exponent $\beta(z)$ and local light cone exponent $\gamma(z)$ with local hopping exponent $\alpha(z)$.

C. Algebraic localization and crossover

Band edges in the spectral function $J(\omega)$ are essential for realizing photonic bound states when the emitter is tuned *outside* the band. In the absence of any waveguide modes resonant with the emitter, spontaneous emission is suppressed and any initial excitation of the emitter instead hybridizes into a dressed eigenstate (a.k.a. bound-state) of a photon shared between emitter and waveguide, with the photonic part of the bound state wavefunction residing in the waveguide due to coupling between the emitter and the band-edge(s) (essentially the modes with v_g near zero). In all waveguide-QED platforms studied to date, this bound-state is exponentially localized around the emitter[1]. In contrast, the long range nature of left-handed waveguide leads to a qualitatively different nature of localization leading to *extended* bound-states with an algebraic (power-law) tail.

To show this, we follow the standard procedure of calculating the bound-state energy. Considering the general

single-excitation eigenstate of the full Hamiltonian,

$$|\psi_{\text{bound}}\rangle = C_e |e, 0\rangle + \sum_k C_k a_k^\dagger |g, 0\rangle, \quad (10)$$

such that $H|\psi_{\text{bound}}\rangle = E_{\text{bound}}|\psi_{\text{bound}}\rangle$, leads to the following transcendental equation for the bound-state energy

$$E_{\text{bound}} = \Delta + \Sigma(E_{\text{bound}}), \quad \Sigma(E) = \sum_k \frac{|g_k|^2}{E - \omega_k}, \quad (11)$$

where $\Sigma(E)$ is the self-energy function of the system (see Supplementary Materials for the functional form). Real solutions to this equation outside the continuum, i.e. $E_{\text{bound}} \in \mathbb{R} \setminus [\omega_{\text{IR}}, \omega_{\text{UV}}]$ determine the existence of qubit-photon bound-states. The average photon number at site n in real space is obtained by Fourier transforming the coefficients C_k as,

$$\begin{aligned} \langle \psi_{\text{bound}} | a_n^\dagger a_n | \psi_{\text{bound}} \rangle &\equiv \langle a_n^\dagger a_n \rangle \\ &= |C_e|^2 \left| \frac{g}{2\pi} \int_{-\pi}^{\pi} dk \frac{e^{-ikn}}{E_{\text{bound}} - \omega(k)} \right|^2, \end{aligned} \quad (12)$$

where the final expression is obtained in the continuum- k limit ($N \rightarrow \infty$) such that the unit-cell size, and consequently k_{max} , remain finite. The normalization $|C_e|^2$ is set by demanding a normalized bound-state wavefunction. For positions far away from the qubit location ($n \gg 1$), we can analytically evaluate the bound-state profile as,

$$\langle a_n^\dagger a_n \rangle \simeq \frac{g^2 |C_e|^2}{\pi^2 \omega_0^2 n_*^2} \left(\frac{K_1(n/n_*)}{n} \right)^2, \quad (13)$$

This analytical result is consistent with the numerical results obtained via an exact diagonalization of single-excitation Hamiltonian. Interestingly, when the bound-state energy is sufficiently far away from the band-edge, this results remains surprisingly accurate even for relatively small n (see Supplementary Materials).

1. Extended bound states

Remarkably, unlike the usual exponentially localized bound states, the bound state in LHTL waveguide-QED system exhibits a long power-law tail. In fact, for infinite cutoff, $\omega_c \rightarrow \infty$ or $n_* \rightarrow \infty$, the bound state exhibits an exact algebraic profile with quartic fall-off with distance from the emitter (Fig. 3A),

$$\langle a_n^\dagger a_n \rangle = \frac{g^2 |C_e|^2}{\pi^2 \omega_0^2} \left(\frac{1}{n^4} \right), \quad (14)$$

where we have used $K_1(z) \approx 1/z$ for $z \ll 1$. Figure 3B shows the bound state profiles calculated as a function of n_* , which show that the algebraic profile persists up to $n \ll n_*$, and modifies to an Ornstein-Zernike form for $n \gg n_*$,

$$\langle a_n^\dagger a_n \rangle \simeq \frac{g^2 |C_e|^2}{2\pi n_* \omega_0^2} \frac{e^{-2n/n_*}}{n^3} \quad (15)$$

The algebraic localization is a direct consequence of the intrinsic long-range couplings in the LHTL, as evidenced by the strong dependence of bound state profile on $n_* = \omega_{UV}/2\omega_{IR}$, with the bound-state profile being *algebraic* over the regime where the couplings are strong long-range ($n \ll n_*$) and crosses over to an *exponential* tail for $n \gg n_*$, where the couplings themselves are effectively short-range. We establish a direct connection between bound-state profile and the underlying hopping network by deriving an analytic relation between the local hopping exponent, $\alpha(z)$ (see Eq. 9a) and the local bound-state exponent, $\beta(z) \equiv -d \ln |\phi_z|/d \ln z$ with $\phi(z)$ being the un-normalized bound-state amplitude, as

$$\beta^{\text{LH}}(z) = 2 + \frac{z K_0(z)}{K_1(z)} = 2 + \frac{z^2}{\alpha^{\text{LH}}(z)}, \quad (16)$$

Here we have exploited the similar structure of Eqs. 9a and 13, to extend the running exponent method for describing a generic bound-state intensity profile using a position-dependent exponent $2\beta(z)$; as shown in Fig. 3C, it equals 4 for $z < 1$ and scales approximately linearly with distance beyond $z = 1$. A constant local exponent corresponds to a pure power-law behavior while a linear increase with distance implies an exponential fall off.

Since the term $z^2/\alpha(z)$ is strictly positive for any finite n_* (i.e., since $\alpha(z) > 0$), the spatial decay of bound-state amplitude is never slower than n^{-4} . Notably, the crossover point $z = 1$ ($n = n_*$) lies between $z_1 \approx 0.60$ and $z_2 \approx 1.55$, the distances governing the crossover from strong- to weak long-range hopping and from weak long-range to short-range hopping in 1D systems respectively, i.e. $\alpha(z_{1,2}) = 1, 2$, [15].

For comparison, we also show the bound state exponent obtained for the conventional right-handed waveguide-QED system in Fig. 3C (see Supplementary Materials for “calculational” details of RHTL waveguide-QED). In this case, the dispersion is gapless and linear

for $k \rightarrow 0$, i.e., $\omega_k \simeq \omega_0 |k|$. For $\omega_c > \omega_0$, we find, $\xi^{\text{RH}}(n) \simeq \omega_0/\pi n^2$ and $|\phi_n|^2 = (\omega_0^2 g^2/\pi^2 E_{\text{bound}}^4) n^{-4}$ in the limit $n \gg 1$, showing that the resulting hopping network and the qubit-photon bound-state profile are essentially insensitive to ω_{UV} . This is not entirely surprising since the system always operates in the $n_* \rightarrow \infty$ limit since $\omega_{\text{IR}}^{\text{RH}} = 0$. Thus, while the RHTL also exhibits algebraic bound-state profiles, it does so with constant exponents, $\alpha^{\text{RH}}(z) = 2$ and $\beta^{\text{RH}}(z) = 2$ with no crossover (see Fig. 3C).

It is instructive to note that the standard coupled cavity-array picture of waveguide-QED with short-range or nearest-neighbor hoppings, corresponds to the “bad” waveguide limit of LHTL. Specifically, this is realized when $\omega_c \ll \omega_0$ or equivalently $C \gg C_0$, leading to an almost flat dispersion and suppressed hopping between neighboring sites (cavities). In this regime, we reproduce the familiar *exponentially localized* bound-state profiles obtained for nearest-neighbor couplings.

In addition to the n_* -controlled crossover, the bound state has a short-range exponential core around the qubit, with the characteristic length scale $\lambda_{\text{core}} \propto \delta^{-1/2}$, where $\delta = \omega_{\text{IR}} - E_{\text{bound}}$ denotes the detuning of the (dressed) emitter frequency from the band edge [17, 18] (see Supplementary materials). Such frequency-tunable bound state cores, with emitter parked very close to the band-edge, have often been proposed as a mechanism for implementing “long-range” qubit-qubit interactions [5, 10, 11, 19]. The extended bound states reported in our work present a qualitatively distinct paradigm for realizing long-range interactions both in terms of the functional form of the bound state (algebraic vs exponential), as well as the interaction length scale being independent of the emitter frequency and solely determined by the waveguide properties (specifically, $n_* = \omega_{UV}/2\omega_{\text{IR}}$). From a practical design standpoint, extending the range of bound state via tuning of emitter frequency leads to a fine-tuning problem since a small detuning δ also makes the emitter susceptible to be in accidental resonance with modes near the band-edge especially due to coupling-induced Lamb shifts [5].

D. Non-Markovianity and Accelerated Light Cones

In this section, we investigate the effect of native long-range hoppings in the LHTL on the dynamics of scattered photons and qubit population. In the context of former, we will see how LHTL waveguide-QED system leads to unconventional light cones with position-dependent exponents, while for the latter it leads to non-Markovian decays for qubit parked inside the continuum ($\omega_{\text{IR}} < \Delta < \omega_{UV}$). As before, we start with a most general single-excitation state, now including the time dependence of wavefunction amplitudes explicitly,

$$|\psi(t)\rangle = C_e(t)|e, 0\rangle + \sum_k C_k(t) a_k^\dagger |g, 0\rangle, \quad (17)$$

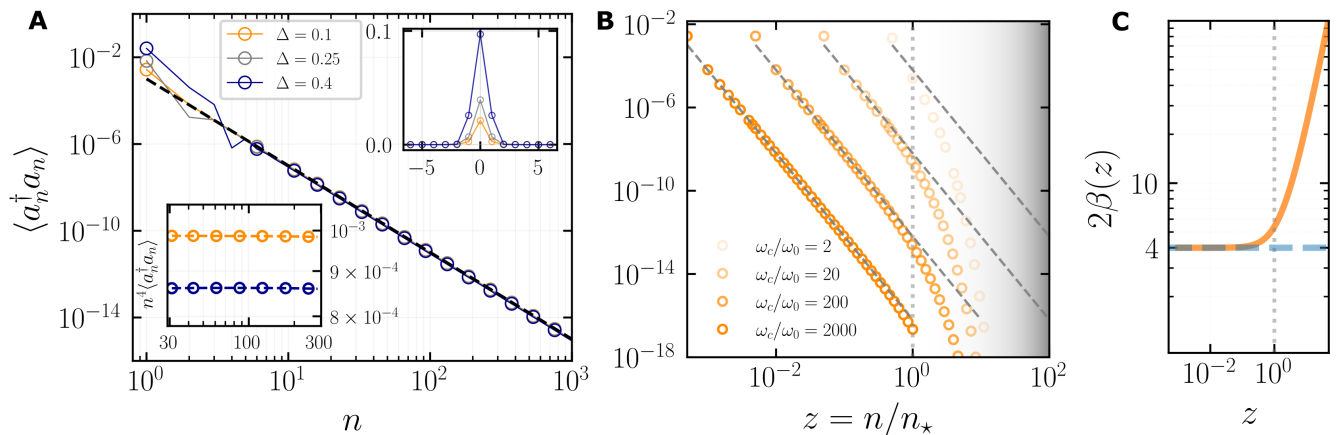


FIG. 3. **Algebraic bound-states in LH waveguide-QED.** **A** Spatial profile of bound state for $n_\star \rightarrow \infty$, for different emitter frequencies ($g/\omega_0 = 0.1$) shown in different color markers. The dashed black line shows the fit to $1/n^4$ power-law. The top-right inset shows the photon intensity profiles near the qubit location for the three cases. The lower-left inset shows a slightly different asymptote values for two different emitter frequencies (detunings). **B** Spatial profiles of bound state, for different values of $\omega_{UV} = \omega_c$, each showing the exponential decay in the region $z > 1$ ($n > n_\star$) (indicated with the gray gradient on the right). **C** Position-dependent local bound state exponent, $2\beta(z)$, for left-handed (solid-orange) and right-handed (dashed-blue) waveguide-QED systems, calculated using the running exponent method.

with $C_e(0) = 1$ and $C_k(0) = 0$.

1. Non-Markovian Qubit Dynamics

Plugging Eq. 17 in time-dependent Schrödinger equation gives a set of coupled differential equations which, after eliminating the photonic mode amplitudes, yields,

$$\dot{\tilde{C}}_e(t) = - \int_0^t K(\tau) \tilde{C}_e(t - \tau) d\tau, \quad (18)$$

where $\tilde{C}_e(t) = e^{i\Delta t} C_e(t)$, and $K(\tau) = (2\pi)^{-1} \int_0^\infty d\omega e^{-i(\omega - \Delta)\tau} J(\omega)$ is the memory kernel. A Markovian bath is modeled as a white spectral density, $J(\omega) \simeq \text{const.}$, which immediately yields a pure-exponential decay of qubit population. For instance, coupled-cavity arrays and even RHTLs present such Markovian baths to qubits parked sufficiently away from the band edges. On the other hand, for the Brownian spectral density for LH TL (Eq. 3), even the deep-in-band dynamics remain highly non-Markovian. The time-non-local equation for qubit population can be solved exactly using analytical continuation in Laplace domain. Here we report the final form for time-domain solution, assuming infinite cutoff $\omega_c \rightarrow \infty$ (see Supplementary Materials for details)

$$\begin{aligned} C_e(t) &= \frac{8g^2}{\pi\omega_0^2} \int_{-\infty}^{-1} dx M(x) e^{i\omega_0 x t/2} + r e^{iy_p t} \\ &\equiv C_e^{(s)}(t) + C_e^{(b)}(t). \end{aligned} \quad (19)$$

Here $C_e^{(b,s)}(t)$ correspond to the bound-state and scattering contributions respectively. The pole denoted by

y_p is obtained as a real-valued solution to the bound-state energy equation, $y + \Delta + \Sigma(-y) = 0$, with the corresponding residue, $r = [1 - \Sigma'(-y_p)]^{-1}$. As evident from the contour shown in Fig. 4A, the dominant contribution to $C_e^{(s)}(t)$ coming from the integration about the ‘continuum branch cut’ shown in red. We refer the function $M(x)$, plotted in Fig. 4B, as the spectral weight function which shows a peak near the dressed qubit frequency. Since $C_e^{(s)}(\infty) = 0$, the steady-state solution is entirely governed by the contribution from the bound state, $|C_e(\infty)|^2 = |r|^2$.

Finite-time population dynamics are a combination of both scattering and bound-state contributions, though the functional form of decay envelope is dominated by the scattering contribution $C_e^{(s)}(t)$ as different time scales selectively probe different regions of the spectral weight function $M(x)$ (see Fig. 4C). We analyze the scattering contribution $C_e^{(s)}(t)$ in three limiting cases.

(i) At very short times, $\max_k |\omega(k) - \Delta| t \ll 1$, Eq. 18 gives the universal quadratic decay,

$$|C_e^{(s)}(t)|^2 \approx 1 - (\Gamma t)^2, \quad (20)$$

where $\Gamma = (2\pi)^{-1} \int d\omega J(\omega)$. This ‘Zeno window’ always exists, but its span shrinks as the ω_{UV} increases.

(ii) In the infinite-cutoff limit, the decay begins with a Wigner-Weisskopf-type exponential for $0 \leq t \lesssim \tau_1 \equiv 1/\gamma$. In this regime, the qubit primarily samples modes near the renormalized (ore dressed) qubit frequency, where $M(x)$ can be well approximated by a Lorentzian (see Fig. 4D). This yields

$$|C_e^{(s)}(t)|^2 \approx \left(\frac{16g^2 |a_0|}{\omega_0^2} \right)^2 e^{-\gamma t}, \quad (21)$$

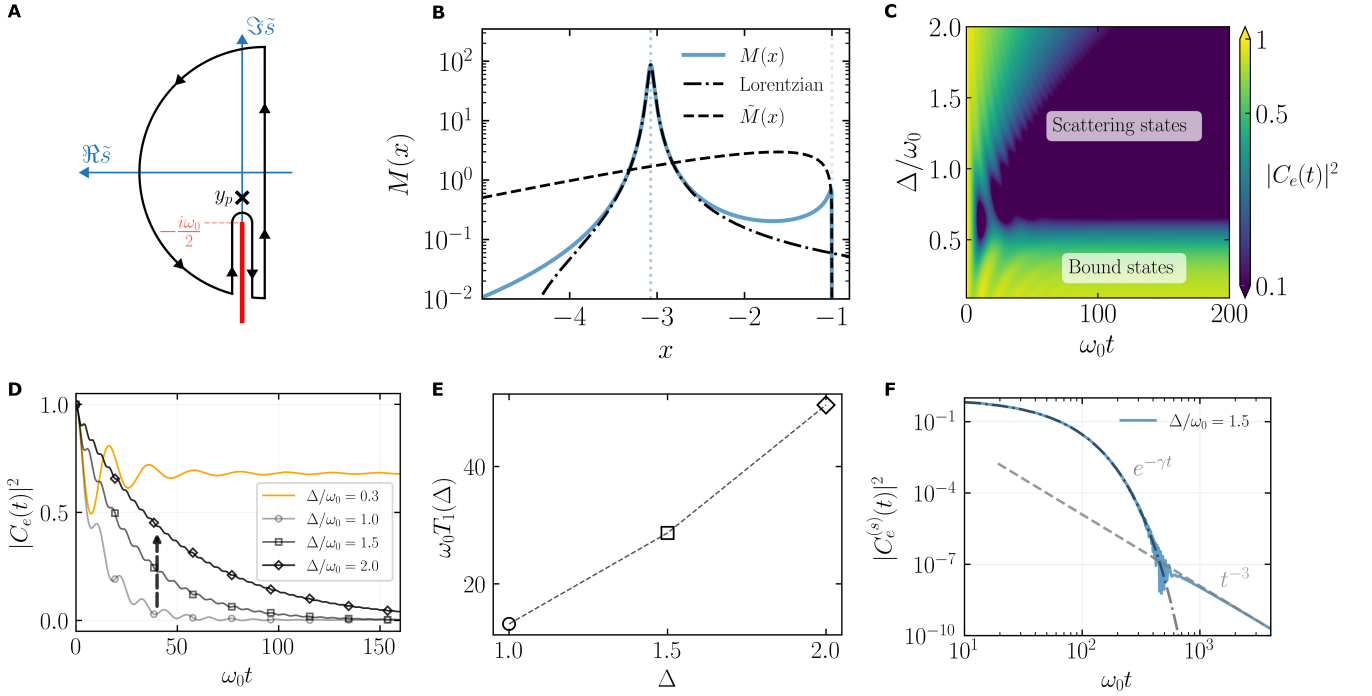


FIG. 4. **Qubit-Dynamics for infinite UV cutoff.** **A** Contour in Laplace \tilde{s} -space used for calculating qubit dynamics. Solid red line and the black cross show the branch cut due to the continuum and bound-state pole y_p outside the continuum, respectively. **B** Profile of spectral weight function $M(x)$ plotted in rescaled frequency units $x (= 2\omega/\omega_0)$, calculated for $\Delta/\omega_0 = 1.5$, $g/\omega_0 = 0.2$. Solid line shows the full function, while patterned lines show the approximations used for capturing the contribution of peak near the dressed emitter frequency ($x \leq 2\Delta/\omega_0$) (dot-dashed) and contributions from the band-edge (dashed line), respectively. **C** Emitter population dynamics for Δ across the LHTL band-edge ($\omega_0/2$). **D** Time-slices at different emitter frequencies taken from (C). The arrow indicates increasing relaxation time with increasing Δ (decreasing decay rate). **E** Relaxation time $T_1 \equiv 1/\omega_0\gamma$ analytically calculated at emitter frequencies in (D). **F** Crossover from exponential relaxation $e^{-\gamma t}$ to long-time power-law tail t^{-3} .

with $\gamma > 0$ determined by Δ , and $a_0 \in \mathbb{C}$ is an overall complex detuning-dependent prefactor (see Supplementary Materials). Interestingly, qubit decay rate γ decreases with increasing qubit frequency (see black arrow), a direct consequence of inverted spectral density ($J(\omega) \sim 1/\omega^2$) of the LHTL (Fig. 4E).

(iii) At late times, $t \gg \tau_2$, the region near $x = -1$ [20] becomes important where $M(x)$ shows a sharp discontinuity, since rapid oscillations suppress all contributions except those from the lower band-edge. Approximating $\tilde{M}(x) \simeq M(x \approx -1)$ in this regime gives the long t^{-3} tail, as shown in Fig. 4F (see Supplementary Materials),

$$|C_e^{(s)}(t)|^2 \approx \frac{1}{16\pi} \left(\frac{\omega_0}{g}\right)^4 \frac{1}{(\omega_0 t)^3}. \quad (22)$$

As noted in [20], there is also an intermediate window $\tau_1 < t < \tau_2$ when the population decays as t^{-1} , arising from the contribution of the smaller shoulder near the band edge at $x = -1$ which becomes increasingly sharp as $g \rightarrow 0$. If on the other hand, the qubit is parked outside the continuum, see Fig. 4, a bound-state is formed leading to fractional decay of population at long times.

2. Photon Dynamics: accelerated light cones

Long-range couplings and interactions are known to profoundly modify the propagation of excitations and correlations in many-body systems [21–24]. Specifically, the long-range lattice models can exhibit a gamut of distinct propagation phenomena, ranging from non-local spreading of correlations in strong long-range models to quasi-local propagation (nonlinear light cones). Given the challenges imposed by nonlocal nature of such models, only recently, the optimal bounds on interaction exponents, $\alpha > 2(3)$ in non-interacting (interacting), required for linear light cones in long range models have been reported [25].

As shown earlier, LHTL realizes a ‘running’ hopping exponent $\alpha(z)$, which makes it a unique system to access all these regimes in a single setup probed at different length scales. In this section, we delineate these different regimes by introducing the notion of a ‘running’ light-cone exponent in LHTL waveguide-QED system. To this end, we calculate the spatial amplitude of scattered photons as the inverse Fourier transform of $C_k(t)$ (Eq. 17),

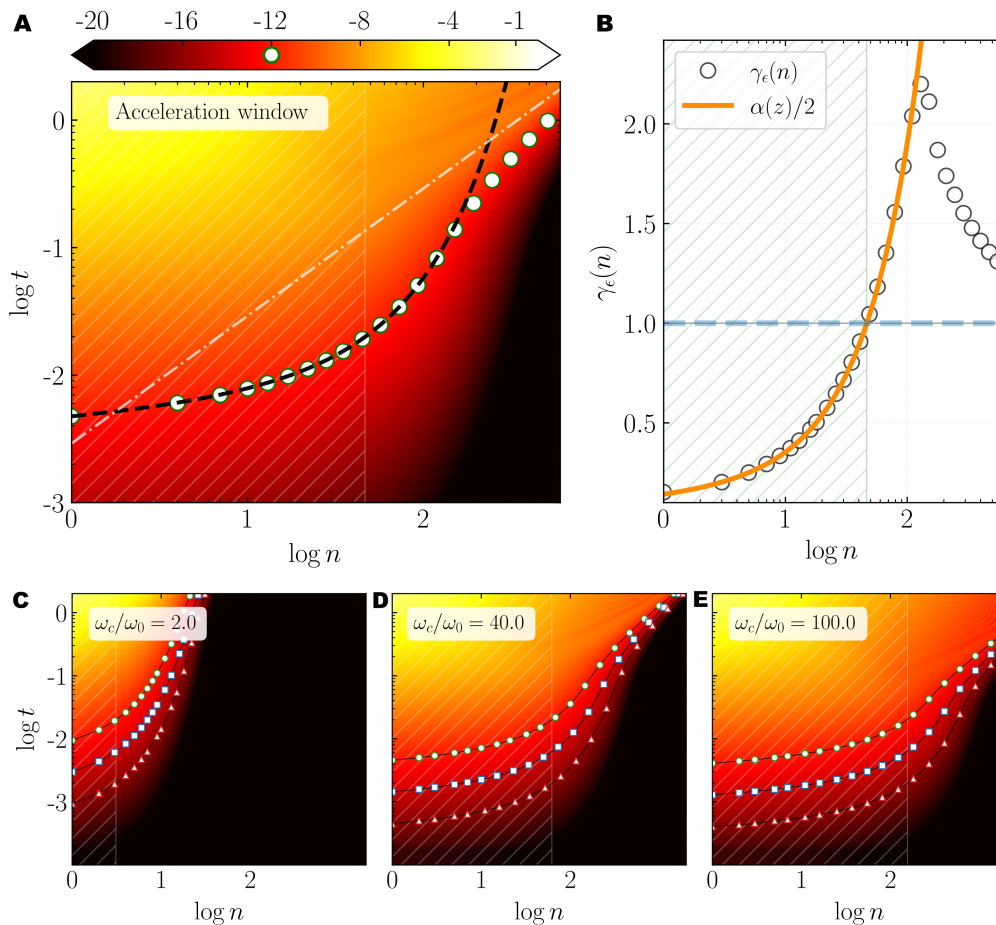


FIG. 5. **Accelerated light cones in LH waveguide-QED.** **A** Simulated space-time diagrams of photon intensity $\ln |C_n(t)|^2$ for a qubit parked inside the pass band of LHTL ($\Delta/\omega_0 = 1$, $\omega_c/\omega_0 = 30$, $g/\omega_0 = 0.08$). Simulated constant intensity fronts, $t_\epsilon(n)$ for $\epsilon = 10^{-12}$, are plotted as solid white-circles ($N = 1501$), while the short-time analytical result is shown with the dashed-black line. Dot-dashed white line corresponds to the linear light cone $t = n/v_{\max}$. **B** Empty circles represent the local slope for light-cone obtained from simulations, and the solid-orange curve represents the analytical result obtained in Eq. 26. **C,D,E** show the space-time density profiles of scattered photons within the accelerated windows for three different choices of n_* = 2, 40, 100. In each density plot, circle, square, and triangle markers show ϵ -fronts for three different choices of $\log(\epsilon) = -12, -14, \text{ and } -16$, respectively ($N = 4001$).

as

$$\begin{aligned} C_n(t) &= \frac{g}{2\pi} \int_{-\pi}^{\pi} dk e^{ikn} \left(\int_0^t d\tau e^{-i(t-\tau)\omega(k)} C_\epsilon(\tau) \right) \\ &= g \int_0^t d\tau G_n^R(t-\tau) C_\epsilon(\tau) \end{aligned} \quad (23)$$

where in the second equation, the photon amplitude has been re-cast into an manifestly time-delayed form using the retarded photon propagator,

$$\begin{aligned} G_n^R(t) &\equiv -i\Theta(t) \langle [a_n(t), a_0^\dagger(0)] \rangle \\ &= (2\pi)^{-1} \int_{-\pi}^{\pi} dk e^{ikn - i\omega(k)t}. \end{aligned} \quad (24)$$

For non-interacting bosonic systems, bounds on particle propagation have been derived using state transfer protocols or quantum walks on d -dimensional lattices [25].

Here, we adopt a different route in order to maintain a thematic connection with position-dependent hopping network derived earlier; to this end, we analyze photon propagation in LHTL waveguide-QED systems by tracking constant-intensity photonic fronts which we henceforth allude to as ϵ -fronts. We identify $t_\epsilon(n)$ as the earliest time an intensity threshold ϵ is reached at a distance n along the transmission line. In other words, $t_\epsilon(n)$ tracks the iso-intensity curve in (n, t) -plane, i.e., $|C_n(t)|^2 = \epsilon$. To get some analytical handle on the dynamics, for very short-times we can approximate $C_\epsilon(\tau) \approx 1$, and expand $G_n^R(t) \simeq -\xi_n t + O(t^2)$, yielding a direct relationship between the emitted field and the hopping network of the transmission line,

$$C_n(t) \simeq -\frac{ig}{2} \xi_n t^2, \quad (25)$$

where ξ_n is the hopping network (Eq. 5). The ϵ -fronts are

obtained as $t_\epsilon(n) = (2\epsilon/g) \xi_n^{-1/2}$ (Fig. 5A), from which we can derive the local light-cone exponent as

$$\gamma_\epsilon^{\text{LH}}(z) \equiv \frac{d \ln t_\epsilon(z)}{d \ln z} = \frac{\alpha^{\text{LH}}(z)}{2}. \quad (26)$$

In 1D free long-range hopping models with constant $1/r^\alpha$, the light cone is rigorously shown to be linear when $\alpha > d + 1 = 2$, and no linear cone exists for $1 < \alpha < 2$ [25]. For $\alpha < 1$, the dynamics are non-local with the details of propagation highly dependent on the choice of model. However, the LH TL hopping network is not constant- α —its exponent $\alpha(z)$ grows with distance and crosses $\alpha = 1, 2$ at $z_1 \approx 0.60$, and $z_2 \approx 1.55$ (Fig. 5B). Accelerated fronts appear in the region $z < z_2$, where $\alpha(z) < 2$ or $\gamma < 1$. Once $\alpha(z) > 2$, $\gamma \rightarrow 1$, the fronts cease to accelerate and align with the linear cone set by $v_{\text{max}} = \max_k v_g(k)$ at large distances. In fact, in simulation we find the ϵ -fronts decelerate for $z > z_2$ saturating to linear cones in the long distance regime. Unsurprisingly, while the crossover into decelerating light cones is captured by short-time analytics, the long distance saturation to $\gamma = 1$ requires going beyond the linear approximation to $G_n^R(t)$.

This analysis shows that the free light cone bounds derived for systems with constant- α apply locally to the scale-dependent light-cone exponent $\gamma(z)$, which changes continuously as the photon propagates through an LH TL. As all distances z are defined w.r.t. $n_\star = \omega_{\text{UV}}/(2\omega_{\text{IR}})$, as in the case of bound state localization, the interplay of UV and IR cutoffs controls the distance over which the accelerated light cones are realized (Fig. 5C-E). Within the accelerating window ($z < z_2$), we can combine Eq. 16 and 26 to obtain a direct relation between the bound-state and light-cone exponents as,

$$\beta^{\text{LH}}(z) = 2 + \frac{z^2}{2\gamma^{\text{LH}}(z)}. \quad (27)$$

Since, Eq. (26) is independent of the handedness of the transmission line, we can use it to study the light cone exponents in RH TLs too. Since $\alpha^{\text{RH}}(z) = \bar{\alpha}^{\text{RH}}(z) = 2$ (Eq. 9b), the ϵ -cones are linear, $\gamma^{\text{RH}}(z) = \alpha^{\text{RH}}(z)/2 = 1$, at all times. Hence, in contrast to LH TL, $z_2^{\text{RH}} = 0$ implying that there is no region in an RH TL waveguide-QED system where the free light cones are super-linear or accelerated (see Supplementary Materials). This is in alignment with the extended Lieb-Robinson bounds for systems with power-law hopping [25] which predict that a finite-sized acceleration window ($\gamma < 1$) requires hopping that decays *slower* than at least $1/n^2$ ($\alpha < 2$) over that distance. The RH TL case with $\xi_n \sim 1/n^2$ is in the marginal, non-accelerating limit.

E. Robustness of the long-range physics to coupling structure

Most theoretical treatments of standard waveguide-QED consider spatially local emitter-waveguide coupling,

while ignoring its resultant momentum-dependence. This assumption is strictly true only for weak coupling to environments with a small dispersion bandwidths. Even in the presence of structured environments, specifically which lead to a non-white or ‘colored’ $J(\omega)$, such an approximation maybe more forgiving for calculating emission properties, such as relaxation rates, where the density of states near resonance with the emitter dictate the dynamics. Over such narrow spectral windows, one can always make a linear expansion of dispersion near the relevant frequency leading to a ‘white’ $J(\omega)$. The validity of such an approach, however, remains in question when calculating properties of bound states that are determined by the global structure (‘poles’) of the self-energy function (Eq. 11). Moreover, such local approximations may fail even for scattering properties when propagation over extended distances is relevant, such as, for calculation of light cone exponents or relaxation of atoms in situations which fall outside the purview of standard dipole approximation (e.g., giant atoms[2], phononic baths etc.). The structural non-Markovianity and native long-range nature of transmission line-based waveguide-QED systems, makes it seem more imperative to revisit the assumption of assuming of flat g_k for both RH TL and LH TL cases. In this section., we explicitly take into account to calculate the effect of momentum-dependence of g_k and quantify its effect on both bound state exponent $\beta(z)$ and light cone exponent $\gamma(z)$.

Using a detailed microscopic derivation, we find (see Supplementary Materials),

$$g^{\text{LH}}(k) = g_0 \left(\frac{C_0}{C} \right)^{1/2} \left(\frac{\omega(k)}{\omega_0} \right)^{3/2}, \quad (28)$$

$$g^{\text{RH}}(k) = g_0 \left(\frac{\omega(k)}{\omega_0} \right)^{1/2},$$

where $g_0 = (C_c/2\sqrt{N})\sqrt{\omega_q\omega_0/(C_qC_0)}$. This leads to a strong modification of the spectral function profile for LH TL,

$$J_{g_k}(\omega) = \frac{2g_0^2\omega_0^2}{\sqrt{1 - \left[1 - \frac{\omega_0^2}{2} \left(\frac{1}{\omega^2} - \frac{1}{\omega_c^2} \right) \right]^2}}, \quad (29)$$

which changes its profile from Brownian $J(\omega) \sim 1/\omega^2$ (Eq. 3b) to Ohmic $J(\omega) \sim \omega$ away from the band edges. This inverts the frequency dependence of the relaxation rates, reported in Eq. 21 (cf. Fig. 4E).

The more pertinent quantities of interest from the perspective of long-range waveguide-QED are the respective bound state profiles and light cone shapes. One can presage the expected modification here by noting that while the couplings grow with increase in frequency in both cases, they can have distinct and even opposing effects on extended spatial behavior due to opposite nature of dispersion in the two TL systems: while in LH TL this boosts the participation of long-wavelength modes,

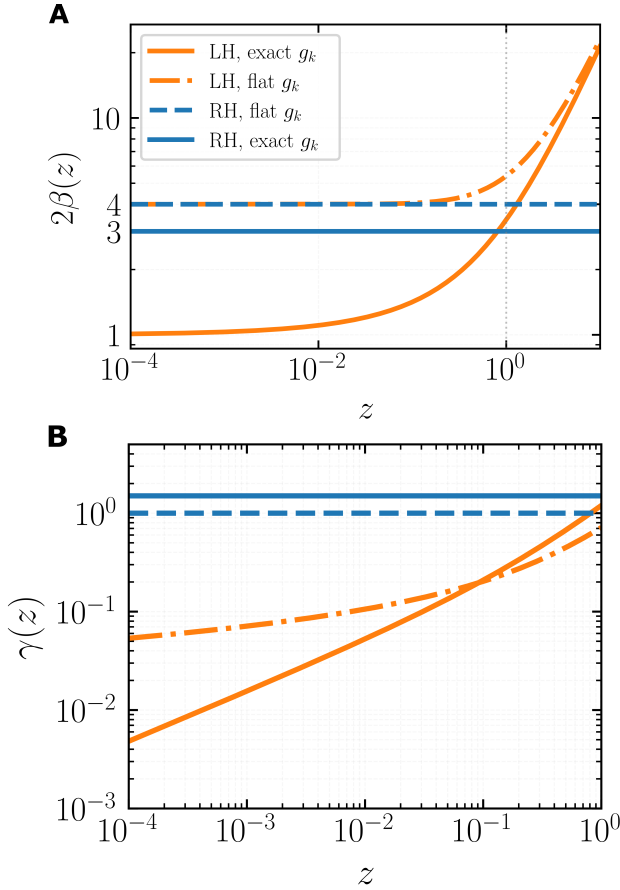


FIG. 6. **Effect of momentum-dependent emitter-waveguide coupling:** **A** Bound-state exponent $2\beta(z)$ for flat (dashed) vs momentum-dependent (solid) coupling constant. The long-range nature of LHRTL manifests in position-dependent exponents obtained for both cases (orange), while RHRTL shows constant-exponent power-law behavior in both cases (blue). **B** Light-cone exponents $\gamma(z)$ calculated for short-time regime. Faster acceleration is obtained with $g(k)$, as compared to constant coupling, for LHRTL (orange) while the reverse is true for RHRTL (blue). Interestingly, there is a crossover at $z \approx 0.1$, which implies that over distances in the range $0.1 < z < z_2$ the flat g cones are more accelerated than their momentum-dependent counterparts. Such a crossover is not present in case of localization exponents.

in RHRTL it privileges short-wavelength contributions instead. An explicit calculation of site-dependent photon number, now including generic momentum-dependent $g(k)$,

$$\langle a_n^\dagger a_n \rangle = |C_\epsilon|^2 \left| \frac{1}{2\pi} \int_{-\pi}^{\pi} dk \frac{g(k) e^{-ikn}}{E_{\text{bound}} - \omega(k)} \right|^2. \quad (30)$$

leads to a modified bound-state profile and local expo-

nent for LHRTL,

$$\langle a_n^\dagger a_n \rangle^{\text{LH}} = \frac{\omega_0 g_0^2 |C_\epsilon|^2}{4\pi^{5/2} n_*^{3/2} \varpi} \left(\frac{K_{1/4}(n/n_*)}{n^{1/4}} \right)^2, \quad (31)$$

$$\beta^{\text{LH}}(z) = \frac{1}{2} + z \frac{K_{3/4}(z)}{K_{1/4}(z)},$$

where $\varpi \approx 2.622$ is the Lemniscate constant that commonly appears while evaluating Elliptic integrals. Interestingly, compared to Eq. (16), including the momentum-dependence of $g(k)$ leads to a significantly lower local bound-state exponent $\beta(z)$ for $z \ll 1$ (Fig. 6A). This implies an even weaker bound-state localization with LHRTL waveguide, that exhibits a spatial rolloff as $1/n$ instead of $1/n^4$, which can be attributed to an enhanced participation of high-frequency or large-wavelength modes. A similar calculation for the RHRTL yields,

$$\langle a_n^\dagger a_n \rangle^{\text{RH}} = \left(\frac{\omega_0 g_0^2 |C_\epsilon|^2}{16\pi^2 E_{\text{bound}}^2} \right) \frac{1}{n^3}, \quad \beta^{\text{RH}}(z) = \frac{3}{2}. \quad (32)$$

As before, RHRTL waveguide-QED system still realizes a power-law localization, though with a diluted constant exponent of 3 ($\forall z$) as compared to that obtained for flat coupling profiles.

Similar treatment for LHRTL light cone exponents yields,

$$t_\epsilon^{\text{LH}}(n) = \frac{\epsilon}{n^{1/4} K_{1/4}(n/n_*)}, \quad \gamma_\epsilon^{\text{LH}}(z) = z \frac{K_{3/4}(z)}{K_{1/4}(z)} \quad (33)$$

showing enhanced acceleration, as reflected in numerically smaller values of $\gamma(z)$ compared to those obtained for the flat g (Fig. 6B). For RHRTL case, the light cones are decelerated at all distances (up to valid short-time regime), as $\gamma_{\text{RH}}(z) = 3/2 > 1$, due to momentum dependence of couplings. Comparing the expressions in Eq. 31, and 33 again yields a relation between the bound-state and light-cone exponents,

$$\beta^{\text{LH}}(z) = \frac{1}{2} + \gamma^{\text{LH}}(z), \quad (34)$$

which is surprisingly simpler compared to the expression in Eq. 27 obtained for momentum-independent coupling g .

III. DISCUSSION

In summary, we showed that transmission line waveguide-QED systems emulate *native* long-range photonic hopping networks that can support new bound-state localization phenomena. While RHRTL maps to a tight-binding lattice with hoppings that decay quadratically with distance, LHRTL systems in contrast show a logarithmic decay of hoppings upto a length scale $n_* = \omega_{\text{UV}}/2\omega_{\text{IR}}$.

It is worth noting that in most waveguide-QED studies, photon localization and photon propagation are treated as independent phenomena. Here, using the running-exponent method we derive analytical relationships between the bound state local exponent extracted from spatial profile of localized wavefunction and light cone exponent extracted from light fronts of scattered photons respectively, both for flat (momentum-independent) and structured (momentum-dependent) emitter-waveguide coupling (Eqs. 27, and 34). Crucially, the crossover from algebraic to exponential bound-state localization as well as from accelerated to linear propagation fronts is set by the scale n_* , making it a unique knob to tune interaction range in LHTL waveguide-QED systems.

Employing the language of running exponents for analyzing TL-based waveguide-QED also allows us to contrast the distinctions between constant-exponent (RHTL) and running-exponent (LHTL) hopping networks. Interestingly, this clarifies that a simultaneous presence of both these phenomena is predicated on realizing strong long-range couplings, a regime inaccessible in RHTL; thus RHTL waveguide-QED exhibits only linear light cones even though it realizes scale-invariant power-law localization. Our results are in direct agreement with the free light cone bounds derived for non-interacting power-law systems, using a single-particle state transfer picture [25].

Our findings constitute a paradigmatic change in waveguide-QED and offer several immediate extensions: most foundational results in single-excitation regime are derived for short-range waveguide models, such as coupled-cavity arrays, and need to be revisited for in-

trinsically long-range waveguides. Further, structural non-Markovianity and accelerated photon scattering (e.g. super-radiance and sub-radiance) in such systems can lead to strong modifications of multi-photon cooperative effects such as super- and sub-radiance, and time-delayed feedback control [26]. Multi-emitter LHTL systems with tunable power-law exchange interactions can lead to new capabilities for analog quantum simulations [5, 27] of many-body models (eg. extended Bose-Hubbard, long-range spin chains), and help explore new dynamical regimes in engineered open quantum systems and unconventional spin-boson models.

From an application perspective, since superconducting LHTLs have already been experimentally demonstrated [28], the proposed platform is within reach of current circuit-QED capabilities and qualitative signatures identified here accessible to experimental tests in the near future. Beyond serving as unconventional waveguides, nonlinear LHTLs embedded with Josephson junctions have already attracted growing interest as a new class of traveling-wave parametric amplifiers due to their exceptional gain characteristics [29]. Additionally, topological edge states in nonlinear LHTLs have also been exploited for efficient higher harmonic generation [30]. This suggests a broad design space available to microwave waveguide-QED systems via a combination of dispersion, nonlinearity and topological properties. Leveraging such platforms to engineer hardware-native nonlocal couplings between distant qubits can also serve to alleviate current bottlenecks in wiring and connectivity of distributed quantum networks, enabling new resource-efficient multi-qubit architectures for long-range entanglement distribution [31].

-
- [1] A. S. Sheremet, M. I. Petrov, I. V. Iorsh, A. V. Poshakinskiy, A. N. Poddubny, Waveguide quantum electrodynamics: Collective radiance and photon-photon correlations. *Rev. Mod. Phys.* **95**, 015002 (2023).
 - [2] G. Andersson, B. Suri, L. Guo, T. Aref, P. Delsing, Non-exponential decay of a giant artificial atom. *Nature Physics* **15** (11), 1123–1127 (2019).
 - [3] B. Kannan, *et al.*, On-demand directional microwave photon emission using waveguide quantum electrodynamics. *Nature Physics* **19** (3), 394–400 (2023).
 - [4] S. Indrajeet, *et al.*, Coupling a Superconducting Qubit to a Left-Handed Metamaterial Resonator. *Phys. Rev. Appl.* **14**, 064033 (2020).
 - [5] X. Zhang, E. Kim, D. K. Mark, S. Choi, O. Painter, A superconducting quantum simulator based on a photonic-bandgap metamaterial. *Science* **379** (6629), 278–283 (2023).
 - [6] A. Ferreri, D. E. Bruschi, F. K. Wilhelm, Particle creation in left-handed metamaterial transmission lines. *Phys. Rev. Res.* **6**, 033204 (2024).
 - [7] D. J. Egger, F. K. Wilhelm, Multimode Circuit Quantum Electrodynamics with Hybrid Metamaterial Transmission Lines. *Phys. Rev. Lett.* **111**, 163601 (2013).
 - [8] A. Ferreri, F. K. Wilhelm, Quantum simulation in hybrid transmission lines. *Phys. Rev. Appl.* **23**, 024026 (2025).
 - [9] M. Mirhosseini, *et al.*, Superconducting metamaterials for waveguide quantum electrodynamics. *Nature Communications* **9** (1), 3706 (2018).
 - [10] E. Kim, *et al.*, Quantum Electrodynamics in a Topological Waveguide. *Phys. Rev. X* **11**, 011015 (2021).
 - [11] M. Scigliuzzo, *et al.*, Controlling Atom-Photon Bound States in an Array of Josephson-Junction Resonators. *Phys. Rev. X* **12**, 031036 (2022).
 - [12] F. Otterpohl, P. Nalbach, E. Paladino, G. A. Falci, M. Thorwart, Quantum $1/f^n$ Noise Induced Relaxation in the Spin-Boson Model. *Phys. Rev. Research* **7**, L042030 (2025).
 - [13] P. Bak, C. Tang, K. Wiesenfeld, Self-organized criticality: An explanation of the $1/f$ noise. *Phys. Rev. Lett.* **59**, 381–384 (1987).
 - [14] A. G. Moghaddam, D. Chernyavsky, C. Morice, J. van Wezel, J. van den Brink, Engineering spectral properties of non-interacting lattice Hamiltonians. *SciPost Phys.* **11**, 109 (2021).
 - [15] N. Defenu, *et al.*, Long-range interacting quantum systems. *Rev. Mod. Phys.* **95**, 035002 (2023).

- [16] C. Cohen-Tannoudji, J. Dupont-Roc, G. Grynberg, *Photons and Atoms: Introduction to Quantum Electrodynamics* (Wiley) (1989).
- [17] V. S. Ferreira, *et al.*, Collapse and Revival of an Artificial Atom Coupled to a Structured Photonic Reservoir. *Phys. Rev. X* **11**, 041043 (2021).
- [18] M. Bello, G. Platero, J. I. Cirac, A. González-Tudela, Unconventional quantum optics in topological waveguide QED. *Sci. Adv.* **5** (7) (2019).
- [19] J. S. Douglas, *et al.*, Quantum many-body models with cold atoms coupled to photonic crystals. *Nat. Photonics* **9** (5), 326–331 (2015).
- [20] E. Sánchez-Burillo, D. Zueco, L. Martín-Moreno, J. J. García-Ripoll, Dynamical signatures of bound states in waveguide QED. *Phys. Rev. A* **96**, 023831 (2017).
- [21] M. C. Tran, *et al.*, Lieb-Robinson light cone for power-law interactions. *Physical Review Letters* **127** (16), 160401 (2021).
- [22] M. Cheneau, *et al.*, Light-cone-like spreading of correlations in a quantum many-body system. *Nature* **481** (7382), 484–487 (2012).
- [23] P. Jurcevic, *et al.*, Quasiparticle engineering and entanglement propagation in a quantum many-body system. *Nature* **511** (7508), 202–205 (2014).
- [24] P. Richerme, *et al.*, Non-local propagation of correlations in quantum systems with long-range interactions. *Nature* **511** (7508), 198–201 (2014).
- [25] M. C. Tran, *et al.*, Hierarchy of linear light cones with long-range interactions. *Physical Review X* **10** (3), 031009 (2020).
- [26] A. L. Grimsmo, Time-Delayed Quantum Feedback Control. *Phys. Rev. Lett.* **115**, 060402 (2015).
- [27] I. Buluta, F. Nori, Quantum Simulators. *Science* **326** (5949), 108–111 (2009).
- [28] H. Wang, *et al.*, Mode Structure in Superconducting Metamaterial Transmission-Line Resonators. *Phys. Rev. Appl.* **11**, 054062 (2019).
- [29] C. Kow, V. Podolskiy, A. Kamal, Self-phase-matched broadband amplification with a left-handed Josephson transmission line. *Phys. Rev. Appl.* **24**, 024026 (2025).
- [30] Y. Wang, L.-J. Lang, C. H. Lee, B. Zhang, Y. D. Chong, Topologically enhanced harmonic generation in a nonlinear transmission line metamaterial. *Nat. Commun.* **10** (1), 1102 (2019).
- [31] S. Singh, *et al.*, Modular architectures and entanglement schemes for error-corrected distributed quantum computation. *npj Quantum Information* **12** (1) (2025).

ACKNOWLEDGMENTS

P.G. would like to acknowledge Saptarshi Biswas for insightful discussions.

Funding: This research was supported by National Science Foundation under grant number DMR-2508447 (P.G.), Defense Advanced Research Projects Agency (DARPA) Synthetic Quantum Nanostructures (SynQuaNon) program under grant number HR00112420343 (J.L.), and Department of Energy under grant DE-SC0019461 (C.A.G-G.). C.A.G-G acknowledges financial support from SECIHTI Mexico, under grant number CBF2023-2024-2888, and DGAPA-PAPIIT-UNAM under grant number IA104625.

Author contributions: P.G. is a graduate student, J.L. and C.A.G.G. are postdoctoral associates, and A.K. is the principal investigator on the project.

Competing interests: There are no competing interests to declare.

Data and materials availability: All data needed to evaluate the conclusions in the paper are present in the paper and/or the Supplementary Materials. Additional data related to this paper may be requested from the authors.

Supplementary Materials

- S1. Full Circuit Quantization of LHTL and RHTL.
- S2. Self-energy: Decay Rate and Lamb Shift.
- S3. Algebraic Bound-state envelope.
- S4. Bound-state core exponential drop: waveguide QED near the band-edge.
- S5. Dispersion reproduction by extended hopping: LHTL and RHTL.
- S6. Exact Dynamics: Inverse Laplace Integration.
- S7. Numerical Diagonalization for bound-state.
- S8. Numerical Diagonalization for dynamics.
- S9. Light-cone expression.
- Figure S1. Right-handed waveguide-QED.
- Figure S2. Self-energy function.
- Figure S3. LHTL Bound-state core exponential window.
- Figure S4. Dispersion relation.
- Figure S5. Light-cones in LHTL and RHTL.

Supplementary Materials for Long-range waveguide-quantum electrodynamics with left-handed transmission lines

P. Goswami¹, J. Liu¹, C. A. González-Gutiérrez^{2,3}, A. Kamal^{1,2}

¹Department of Physics and Astronomy, Northwestern University, Evanston, IL 60208, USA.

²Department of Physics and Applied Physics, University of Massachusetts, Lowell, MA 01854, USA.

³Instituto de Ciencias Físicas, Universidad Nacional Autónoma de México, Cuernavaca 62210, Mexico

*A. Kamal. Email: archana.kamal@northwestern.edu

This PDF file includes:

- S1. Full Circuit Quantization of LHTL and RHTL
- S2. Self-energy: Decay Rate and Lamb Shift
- S3. Algebraic Bound-state envelope
- S4. Bound-state core exponential drop: waveguide QED near the band-edge
- S5. Dispersion reproduction by extended hopping: LHTL and RHTL
- S6. Exact Dynamics: Inverse Laplace Integration
- S7. Numerical Diagonalization for bound-state
- S8. Numerical Diagonalization for dynamics
- S9. Light-cone expression
- Figure S1. Right-handed waveguide-QED.
- Figure S2. Self-energy function.
- Figure S3. LHTL Bound-state core exponential window.
- Figure S4. Dispersion relation.
- Figure S5. Light-cones in LHTL and RHTL.

S1. CIRCUIT QUANTIZATION FOR LEFT- AND RIGHT-HANDED TRANSMISSION LINES

Quantization of a left-handed transmission line (LHTL)—The left-handed transmission line (LHTL), shown in Fig.1A in the main text, is described by the Lagrangian written in node-flux basis

$$L = \sum_{n=0}^{N-1} \left[\frac{C_0}{2} (\dot{\Phi}_n - \dot{\Phi}_{n-1})^2 + \frac{C}{2} \dot{\Phi}_n^2 - \frac{\Phi_n^2}{2L} \right]. \quad (\text{S1})$$

We consider periodic boundary condition $\Phi_N = \Phi_0$ since we are not interested in boundary effects. Thus, the following analysis becomes exact in thermodynamic limit used in the main text. We introduce the discrete Fourier transform (DFT) from the site basis n to the momentum basis k ,

$$\Phi_n = \frac{1}{\sqrt{N}} \sum_k e^{inkd} \tilde{\Phi}_k, \quad k \in \left[-\frac{\pi}{d}, \frac{\pi}{d} \right) \quad (\text{S2})$$

where N is the number of lattice sites, d is the unit-cell spacing, and the allowed momenta lie in the first Brillouin zone with spacing $\Delta k = 2\pi/Nd$. As we show later, in k space, the Lagrangian will be diagonalized. To this end, we define the flux vector $\Phi = [\Phi_0, \Phi_1, \dots, \Phi_{N-1}]^\dagger$, the Lagrangian can be compactly written as

$$L = \frac{1}{2} \dot{\Phi}^\dagger \mathbf{V} \dot{\Phi} - \frac{1}{2L} \Phi^\dagger \Phi \quad (\text{S3})$$

where the matrix \mathbf{V} is given by

$$\mathbf{V} = C_0 \begin{pmatrix} 2+\eta & -1 & & \cdots & -1 \\ -1 & 2+\eta & -1 & & \\ & -1 & 2+\eta & -1 & \\ & & -1 & 2+\eta & \ddots \\ \vdots & & & \ddots & \ddots & -1 \\ -1 & & & & -1 & 2+\eta \end{pmatrix}_{N \times N} = (2C_0 + C)\mathbb{I}_N - C_0\mathbf{T} - C_0\mathbf{T}^\dagger \quad (\text{S4})$$

with

$$\mathbf{T} = \begin{pmatrix} 0 & 1 & & & 0 \\ & 0 & 1 & & \\ & & & \ddots & \\ & & & 0 & 1 \\ 1 & & & & 0 \end{pmatrix}_{N \times N}, \quad \eta = \frac{C}{C_0}. \quad (\text{S5})$$

The DFT can be expressed in a compact matrix form as $\Phi = \mathbf{U} \tilde{\Phi}$, where the unitary matrix \mathbf{U} takes the following form,

$$\begin{bmatrix} \Phi_0 \\ \Phi_1 \\ \vdots \\ \Phi_{N-1} \end{bmatrix} = \frac{1}{\sqrt{N}} \begin{bmatrix} e^{i \cdot 0 \cdot (-\pi)} & e^{i \cdot 0 \cdot (-\pi + \Delta\varphi)} & \cdots & e^{i \cdot 0 \cdot (\pi - \Delta\varphi)} \\ e^{i \cdot 1 \cdot (-\pi)} & e^{i \cdot 1 \cdot (-\pi + \Delta\varphi)} & \cdots & e^{i \cdot 1 \cdot (\pi - \Delta\varphi)} \\ \vdots & \vdots & \ddots & \vdots \\ e^{i \cdot (N-1) \cdot (-\pi)} & e^{i \cdot (N-1) \cdot (-\pi + \Delta\varphi)} & \cdots & e^{i \cdot (N-1) \cdot (\pi - \Delta\varphi)} \end{bmatrix} \begin{bmatrix} \tilde{\Phi}_{-\frac{\pi}{d}} \\ \tilde{\Phi}_{-\frac{\pi}{d} + \Delta k} \\ \vdots \\ \tilde{\Phi}_{\frac{\pi}{d} - \Delta k} \end{bmatrix}. \quad (\text{S6})$$

where $\Delta\phi = \Delta kd = 2\pi/N$. The Lagrangian in k -space then reads,

$$L = \frac{1}{2} \dot{\tilde{\Phi}}^\dagger \mathbf{U}^\dagger \mathbf{V} \mathbf{U} \dot{\tilde{\Phi}} - \frac{1}{2L} \tilde{\Phi}^\dagger \tilde{\Phi}. \quad (\text{S7})$$

Simplifying the diagonal matrix,

$$\begin{aligned} \mathbf{U}^\dagger \mathbf{V} \mathbf{U} &= \mathbf{U}^\dagger \left[(2C_0 + C)\mathbb{I}_N - C_0\mathbf{T} - C_0\mathbf{T}^\dagger \right] \mathbf{U} = (2C_0 + C)\mathbb{I}_N - C_0\mathbf{U}^\dagger \mathbf{T} \mathbf{U} - C_0\mathbf{U}^\dagger \mathbf{T}^\dagger \mathbf{U}, \\ &= \text{diag}(\{C_k\}) \equiv \mathbf{C} \end{aligned} \quad (\text{S8})$$

where $C_k = 2C_0 + C - 2C_0 \cos(kd)$, and we have used $\mathbf{U}^\dagger \mathbf{T} \mathbf{U} = \text{diag}(\{e^{ikd}\})$, and $\mathbf{U}^\dagger \mathbf{T}^\dagger \mathbf{U} = \text{diag}(\{e^{ikd}\})$. The diagonalized Lagrangian in k -space then takes the form

$$L = \frac{1}{2} \dot{\tilde{\Phi}}^\dagger \mathbf{C} \dot{\tilde{\Phi}} - \frac{1}{2L} \tilde{\Phi}^\dagger \tilde{\Phi} \quad (\text{S9})$$

Hamiltonian in k -space— The Lagrangian in Eq. S9 is expanded as,

$$L = \frac{1}{2} \sum_k C_k \dot{\tilde{\Phi}}_k^\dagger \dot{\tilde{\Phi}}_k - \frac{1}{2L} \tilde{\Phi}_k^\dagger \tilde{\Phi}_k = \frac{1}{2} \sum_k C_k \dot{\tilde{\Phi}}_k \dot{\tilde{\Phi}}_{-k} - \frac{1}{2L} \tilde{\Phi}_k \tilde{\Phi}_{-k}. \quad (\text{S10})$$

where in the last step we used the property $\tilde{\Phi}_k^\dagger = \tilde{\Phi}_{-k}$. The canonical momentum is defined as,

$$\tilde{Q}_k \equiv \frac{\partial L}{\partial \dot{\tilde{\Phi}}_k} = C_k \dot{\tilde{\Phi}}_{-k}, \quad (\text{S11})$$

and after Legendre transforming the Lagrangian to the Hamiltonian, we obtain the diagonalized Hamiltonian for the LHLL,

$$\mathcal{H} = \sum_k \tilde{Q}_k \dot{\tilde{\Phi}}_k - \mathcal{L} = \sum_k \left(\frac{1}{2C_k} \tilde{Q}_k \tilde{Q}_{-k} + \frac{1}{2L} \tilde{\Phi}_k \tilde{\Phi}_{-k} \right). \quad (\text{S12})$$

Quantization and commutation relation— Starting from the Lagrangian

$$L = \frac{1}{2} \dot{\Phi}^\dagger \mathbf{V} \dot{\Phi} - \frac{1}{2L} \Phi^\dagger \Phi, \quad (\text{S13})$$

The canonical momentum vector, which is the charge vector, is given by,

$$\mathbf{Q} = \frac{\partial L}{\partial \dot{\Phi}} = \mathbf{V} \dot{\Phi}, \quad \dot{\Phi} = \mathbf{V}^{-1} \mathbf{Q}. \quad (\text{S14})$$

The Hamiltonian in site- n basis

$$H = \mathbf{Q}^T \dot{\Phi} - L = \frac{1}{2} \mathbf{Q}^T \mathbf{V}^{-1} \mathbf{Q} - \frac{1}{2L} \Phi^\dagger \Phi. \quad (\text{S15})$$

It is natural to quantize the flux and charge variables, $\Phi_n \rightarrow \hat{\Phi}_n$ and $Q_n \rightarrow \hat{Q}_n$, respectively and demand the following commutation relations

$$[\hat{\Phi}_n, \hat{Q}_m] = i\hbar \delta_{nm}. \quad (\text{S16})$$

We aim to derive the commutation relation in k -space, $[\hat{\Phi}_k, \hat{Q}_{k'}]$, to perform the ladder operator quantization. Given the following transformations,

$$\begin{aligned} \Phi_n &= \frac{1}{\sqrt{N}} \sum_k e^{inkd} \tilde{\Phi}_k, & \tilde{\Phi}_k &= \frac{1}{\sqrt{N}} \sum_n e^{-inkd} \Phi_n, \\ \tilde{Q}_k &= C_k \dot{\tilde{\Phi}}_{-k} = \frac{C_k}{\sqrt{N}} \sum_n e^{inkd} \dot{\Phi}_n. \end{aligned} \quad (\text{S17})$$

The relation between $\hat{\Phi}_n$ and Q_n reveals that

$$Q_n = \sum_{n'} \mathbf{V}_{nn'} \dot{\Phi}_{n'}, \quad \dot{\Phi}_n = \sum_{n'} (\mathbf{V}^{-1})_{nn'} Q_{n'}, \quad (\text{S18})$$

Using Eq. S17 it follows

$$\tilde{Q}_k = C_k \frac{1}{\sqrt{N}} \sum_n e^{inkd} \dot{\Phi}_n = C_k \frac{1}{\sqrt{N}} \sum_{n,n'} e^{inkd} (\mathbf{V}^{-1})_{nn'} Q_{n'}. \quad (\text{S19})$$

Since $\mathbf{U}^\dagger \mathbf{V} \mathbf{U} = \mathbf{C}$, we get $\mathbf{V}^{-1} = \mathbf{U} \mathbf{C}^{-1} \mathbf{U}^\dagger$, calculated as,

$$\begin{aligned} (\mathbf{V}^{-1})_{nn'} &= \sum_m (\mathbf{U})_{nm} (\mathbf{C}^{-1})_m (\mathbf{U}^\dagger)_{mn'} = \frac{1}{N} \sum_{m=0}^{N-1} e^{in(-\pi+m\frac{2\pi}{N})} (\mathbf{C}^{-1})_m e^{-in'(-\pi+m\frac{2\pi}{N})} \\ &= \frac{1}{N} \sum_{m=0}^{N-1} (\mathbf{C}^{-1})_m e^{i(n-n')(-\pi+m\frac{2\pi}{N})} \\ &= \frac{1}{N} \sum_k C_k^{-1} e^{ikd(n-n')}, \end{aligned} \quad (\text{S20})$$

where $(\mathbf{U})_{nm} = N^{-1/2} \exp[-in(\pi - 2\pi m/N)]$, for $n, m \in [0, N-1]$ and $(\mathbf{C}^{-1})_m = C_k^{-1}$, for $k = -\frac{\pi}{d} + \frac{2\pi m}{Nd}$. We then calculate the k -space commutation relation

$$\begin{aligned} [\hat{\Phi}_k, \hat{Q}] &= \left[\frac{1}{\sqrt{N}} \sum_m e^{-imkd} \hat{\Phi}_m, C_{k'} \frac{1}{\sqrt{N}} \sum_{n,n'} e^{inkd'} (\mathbf{V}^{-1})_{nn'} \hat{Q}_{n'} \right] \\ &= \frac{1}{N} \sum_{m,n,n'} C_{k'} e^{id(-mk+nk')} (\mathbf{V}^{-1})_{nn'} [\hat{\Phi}_m, \hat{Q}_{n'}] \\ &= \frac{i\hbar}{N} \sum_{n,n'} C_{k'} e^{id(-n'k+nk')} (\mathbf{V}^{-1})_{nn'}. \end{aligned} \quad (\text{S21})$$

Substituting Eq. (S20) above

$$\begin{aligned} [\hat{\Phi}_k, \hat{Q}_{k'}] &= \frac{i\hbar}{N} \sum_{n,n'} C_{k'} e^{i\frac{2\pi}{N}(-n'k+nk')} \left(\sum_{k''} C_{k''}^{-1} \frac{1}{N} e^{id(n-n')k''} \right) \\ &= \frac{i\hbar}{N^2} \sum_{l=-N/2}^{N/2-1} C_{k'} C_{k''}^{-1} \sum_{n,n'} e^{id(-n'k+nk'+nk''-n'k'')} \\ &= \frac{i\hbar}{N^2} \sum_{l=-N/2}^{N/2-1} C_{k'} C_{k''}^{-1} N^2 \delta_{-k',k''} \delta_{-k,k''} = i\hbar C_{k'} C_{-k}^{-1} \delta_{-k,-k'}. \end{aligned} \quad (\text{S22})$$

Since $C_{-k} = C_k$, we get the required commutator

$$[\hat{\Phi}_k, \hat{Q}_{k'}] = i\hbar \delta_{k,k'}. \quad (\text{S23})$$

Ladder Operators—The Hamiltonian is given by

$$\hat{H} = \sum_k \left(\frac{1}{2C_k} \hat{Q}_k \hat{Q}_{-k} + \frac{1}{2L} \hat{\Phi}_k \hat{\Phi}_{-k} \right) \quad (\text{S24})$$

If we define the ladder operator as,

$$\begin{cases} \hat{a}_k \equiv \frac{1}{\sqrt{2\hbar}} \left[\frac{\hat{\Phi}_k}{\sqrt{Z_k}} + i\sqrt{Z_k} \hat{Q}_{-k} \right], \\ \hat{a}_k^\dagger \equiv \frac{1}{\sqrt{2\hbar}} \left[\frac{\hat{\Phi}_{-k}}{\sqrt{Z_k}} - i\sqrt{Z_k} \hat{Q}_k \right] \end{cases}, \quad \text{with } Z_k = \sqrt{\frac{L}{C_k}}, \quad (\text{S25})$$

then it follows

$$\hat{\Phi}_k = \sqrt{\frac{\hbar Z_k}{2}} (\hat{a}_k + \hat{a}_{-k}^\dagger), \quad \hat{Q}_k = \frac{1}{i} \sqrt{\frac{\hbar}{2Z_k}} (\hat{a}_{-k} - \hat{a}_k^\dagger). \quad (\text{S26})$$

Hamiltonian in terms of ladder operator is given as,

$$\begin{aligned}\hat{H}_{\text{LH}} &= \sum_k \left[\frac{1}{2C_k} \frac{1}{i^2} \frac{\hbar}{2Z_k} (\hat{a}_{-k} - \hat{a}_k^\dagger)(\hat{a}_k - \hat{a}_{-k}^\dagger) + \frac{1}{2L} \frac{\hbar Z_k}{2} (\hat{a}_k + \hat{a}_{-k}^\dagger)(\hat{a}_{-k} + \hat{a}_k^\dagger) \right] \\ &= \sum_k \hbar \omega_k \hat{a}_k^\dagger \hat{a}_k.\end{aligned}\quad (\text{S27})$$

where ω_k is the dispersion relation for the LHTL,

$$\omega_k = \frac{1}{\sqrt{LC_k}} = \frac{\omega_0 \omega_c}{\sqrt{\omega_0^2 + 2\omega_c^2(1 - \cos(kd))}} \quad (\text{S28})$$

Transmon qubit capacitively coupled to LHTL— Consider a transmon circuit (qubit) coupled to the transmission line at position $s \in [0, N-1]$. The transmon capacitance is denoted as C_q and the coupling capacitance as C_c , the full circuit Lagrangian is written as,

$$L = \sum_{n=0}^{N-1} \left[\frac{C_0}{2} (\dot{\Phi}_n - \dot{\Phi}_{n-1})^2 - \frac{\Phi_n^2}{2L} \right] + \frac{1}{2} C_q \dot{\phi}^2 + E_J \cos\left(\frac{\phi}{\varphi_0}\right) + \frac{1}{2} C_c (\dot{\Phi}_s - \dot{\phi})^2 \quad (\text{S29})$$

where ϕ denote the transmon flux variable. We will use q (qubit) to present transmon charge variables. Considering weakly coupled qubit, $C_c \ll C, C_0$, we ensure that it does not change the waveguide dispersion, we approximate coupling term in the Lagrangian using,

$$\begin{aligned}Q_n &= \frac{\partial L}{\partial \dot{\Phi}_n} = 2C\dot{\Phi}_n - C\dot{\Phi}_{n+1} - C\dot{\Phi}_{n-1} + C_c(\dot{\Phi}_n - \dot{\phi})\delta_{ns} \approx 2C\dot{\Phi}_n - C\dot{\Phi}_{n+1} - C\dot{\Phi}_{n-1} \\ q &= \frac{\partial L}{\partial \dot{\phi}} = (C_q + C_c)\dot{\phi} - C_c\dot{\Phi}_s \approx (C_q + C_c)\dot{\phi} \approx C_q\dot{\phi},\end{aligned}\quad (\text{S30})$$

allowing us to quantized qubit and LHTL Hamiltonian separately, to give the full Hamiltonian,

$$H = \underbrace{\sum_k \left(\frac{1}{2C_k} \hat{Q}_k \hat{Q}_{-k} + \frac{1}{2L} \hat{\Phi}_k \hat{\Phi}_{-k} \right)}_{\hat{H}_{\text{LH}}} + \underbrace{\frac{1}{2C_q} \hat{q}^2 - E_J \cos\left(\frac{\hat{\phi}}{\varphi_0}\right)}_{\hat{H}_q} - \underbrace{\frac{C_c}{C_q} \hat{q} \dot{\Phi}_s}_{\hat{H}_{\text{int}}} \quad (\text{S31})$$

where \hat{H}_{LH} is given in Eq. S27 and the transmon circuit is truncated to lowest two levels by defining,

$$\hat{q} = \sqrt{\frac{\hbar}{2Z_q}} \frac{1}{i} (\sigma^- - \sigma^+), \quad \hat{\phi} = \sqrt{\frac{\hbar Z_q}{2}} (\sigma^- + \sigma^+), \quad Z_q = \sqrt{\frac{L_q}{C_q}}, \quad (\text{S32})$$

where $L_q = \varphi_0^2/E_J$, as a qubit of frequency ω_q with the Hamiltonian approximated as,

$$\hat{H}_q = \frac{1}{2C_q} \hat{q}^2 - E_J \cos\left(\frac{\hat{\phi}}{\varphi_0}\right) \approx \hbar \omega_q \sigma^+ \sigma^- \quad (\text{S33})$$

For the coupling Hamiltonian, we intentionally keep the form $\dot{\Phi}_s$ in the Hamiltonian, despite that a standard Hamiltonian should only consist of flux and charge variables. Using Eq. S17,

$$\dot{\Phi}_s = \frac{1}{\sqrt{N}} \sum_k e^{-iskd} \tilde{Q}_k \frac{1}{C_k} = \frac{1}{\sqrt{N}} \sum_k e^{-iskd} \frac{1}{C_k} \left[\frac{1}{i} \sqrt{\frac{\hbar}{2Z_k}} (\hat{a}_{-k} - \hat{a}_k^\dagger) \right]. \quad (\text{S34})$$

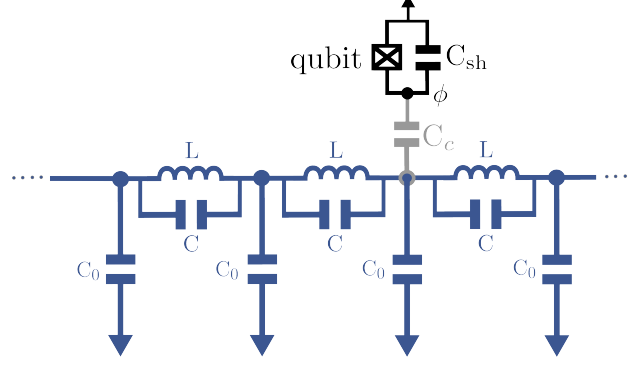


FIG. S1. Right-handed waveguide-QED.

and the coupling term is simplified as,

$$\begin{aligned}
\hat{H}_{\text{int}} &= -\frac{C_c}{C_q} \hat{q} \dot{\Phi}_s \\
&= -\frac{C_c}{C_q} \left(\sqrt{\frac{\hbar}{2Z_q}} \frac{1}{i} (\sigma^- - \sigma^+) \right) \left(\frac{1}{i} \sqrt{\frac{\hbar}{2N}} \sum_k e^{-iskd} \frac{1}{C_k} \sqrt{\frac{C_k}{L}} (\hat{a}_{-k} - \hat{a}_k^\dagger) \right) \\
&= \frac{C_c \hbar}{C_q} \frac{1}{2} \sqrt{\frac{1}{N}} \sum_k \frac{1}{C_k} \sqrt{\frac{C_k}{L}} \sqrt{\frac{C_q}{LJ}} e^{-iskd} (\sigma^- - \sigma^+) (\hat{a}_{-k} - \hat{a}_k^\dagger) \\
&= \sum_k g_k e^{-iskd} (\sigma^- - \sigma^+) (\hat{a}_{-k} - \hat{a}_k^\dagger) \\
&\approx -\sum_k g_k e^{-iskd} (\sigma^- \hat{a}_k^\dagger + \sigma^+ \hat{a}_{-k}) \\
&= -\sum_k \left(g_k e^{-iskd} \sigma^- \hat{a}_k^\dagger + g_k e^{iskd} \sigma^+ \hat{a}_k \right)
\end{aligned} \tag{S35}$$

where we use RWA in the second-last step, $g_{-k} = g_k$ in the last step, and the coupling g_k is given as,

$$g_k = g_0 \left(\frac{C_0}{C} \right)^{1/2} \left(\frac{\omega(k)}{\omega_0} \right)^{3/2}, \quad g_0 = \frac{C_c}{2\sqrt{N}} \sqrt{\frac{\omega_q \omega_0}{C_q C_0}}, \tag{S36}$$

where $\omega_q = 1/\sqrt{C_q L_q}$ is the qubit frequency. The total Hamiltonian of qubit-LHTL then reads,

$$H = \omega_q \sigma^+ \sigma^- + \sum_k \omega_k \hat{a}_k^\dagger \hat{a}_k + \sum_k \left(g_k e^{-iskd} \sigma^- \hat{a}_k^\dagger + g_k e^{iskd} \sigma^+ \hat{a}_k \right) \tag{S37}$$

which is equivalent to Eq. 2 in the main text, where we label $\Delta \equiv \omega_q$ as the emitter frequency.

Quantization of a right-handed transmission line (RHTL)—For RHTL shown in Fig. S1, each unit cell contains an inductor L in series with its associated capacitor C in the main chain, while each node between adjacent LC oscillators is connected to ground via a capacitor C_0 . The Lagrangian for the circuit is

$$L = \sum_{n=0}^{N-1} \frac{C_0}{2} \dot{\Phi}_n^2 + \frac{C}{2} (\dot{\Phi}_n - \dot{\Phi}_{n-1})^2 - \frac{1}{2L} (\Phi_n - \Phi_{n-1})^2. \tag{S38}$$

Both capacitive and inductive energy terms are non-diagonal in position space. In compact matrix form, the Lagrangian can be written as

$$L = \frac{1}{2} \dot{\Phi}^\dagger \mathbf{V}_C \dot{\Phi} - \frac{1}{2} \Phi^\dagger \mathbf{V}_L \Phi, \tag{S39}$$

with

$$\mathbf{V}_C = (C_0 + 2C)\mathbb{I}_N - C\mathbf{T} - C\mathbf{T}^\dagger, \quad \mathbf{V}_L = \frac{1}{L}(2\mathbb{I}_N - \mathbf{T} - \mathbf{T}^\dagger). \quad (\text{S40})$$

The discrete Fourier transform \mathbf{U} simultaneously diagonalizes both matrices \mathbf{V}_C and \mathbf{V}_L . Following the same procedure as in the previous section, the Lagrangian of the RHTL in k -space becomes

$$L = \frac{1}{2} \sum_k \left(C_k \dot{\tilde{\Phi}}_k^\dagger \dot{\tilde{\Phi}}_k - \frac{1}{L_k} \tilde{\Phi}_k^\dagger \tilde{\Phi}_k \right) = \frac{1}{2} \sum_k \left(C_k \dot{\tilde{\Phi}}_k \dot{\tilde{\Phi}}_{-k} - \frac{1}{L_k} \tilde{\Phi}_k \tilde{\Phi}_{-k} \right), \quad (\text{S41})$$

$$C_k = C_0 + C[2 - 2\cos(kd)], \quad L_k = \frac{L}{2 - 2\cos(kd)}.$$

The Hamiltonian is obtained via the Legendre transformation,

$$H = \sum_k \tilde{Q}_k \dot{\tilde{\Phi}}_k - \mathcal{L} = \sum_k \left(\frac{1}{2C_k} \tilde{Q}_k \tilde{Q}_{-k} + \frac{1}{2L_k} \tilde{\Phi}_k \tilde{\Phi}_{-k} \right). \quad (\text{S42})$$

Canonical quantization promotes the dynamical variables to operators and yields a diagonal form,

$$\hat{H} = \hbar \sum_k \omega_k \hat{a}_k^\dagger \hat{a}_k. \quad (\text{S43})$$

The corresponding ladder operators retain the structure given in Eq. (S25), with a different mode-dependent impedance $Z_k = \sqrt{L_k/C_k}$. From the normal-mode parameters one directly obtains the dispersion relation,

$$\omega_k = \sqrt{\frac{1}{C_k L_k}} = \omega_c \sqrt{\frac{1 - \cos(k)}{\frac{\omega_c^2}{2\omega_0^2} + 1 - \cos(k)}}. \quad (\text{S44})$$

where $\omega_0 = 1/\sqrt{LC_0}$ and $\omega_c = 1/\sqrt{LC}$. Using the same procedure, we obtain the coupling strength for the RHTL as,

$$g_k = \frac{C_c}{\sqrt{C_q}} \frac{\hbar}{2} \sqrt{\frac{1}{N}} \sqrt{\omega_q} \sqrt{\omega_k^3 L_k}. \quad (\text{S45})$$

Importantly, for this right-handed circuit the coupling strength g_k cannot be expressed solely as a function of ω_k . This is a direct consequence of the presence of the capacitance C_0 , which introduces an additional k -dependence through C_k and L_k . Nevertheless, in the idealized limit $C = 0$ (equivalently $\omega_c \rightarrow \infty$), one has $C_k = C_0$, $\omega_k = 1/\sqrt{C_0 L_k}$. In this case, the coupling strength simplifies to

$$g_k = g_0 \left(\frac{\omega_k}{\omega_0} \right)^{1/2}, \quad g_0 = \frac{C_c}{2\sqrt{N}} \sqrt{\frac{\omega_q \omega_0}{C_q C_0}}, \quad (\text{S46})$$

which recovers the familiar $\sqrt{\omega_k}$ scaling.

S2. SELF-ENERGY: DECAY RATE AND LAMB SHIFT

The self-energy function $\Sigma(E)$ is given as,

$$\Sigma(E) = \sum_k \frac{|g_k|^2}{E - \omega_k}, \quad g_k \simeq \frac{g}{\sqrt{N}} \quad (\text{S47})$$

A closed form of $\Sigma(E)$ can be calculated in the continuum limit ($N \rightarrow \infty$) all k -sums are expressed in terms of the following integral,

$$\lim_{N \rightarrow \infty} \frac{1}{N} \sum_k \rightarrow \int \frac{dk}{2\pi}. \quad (\text{S48})$$

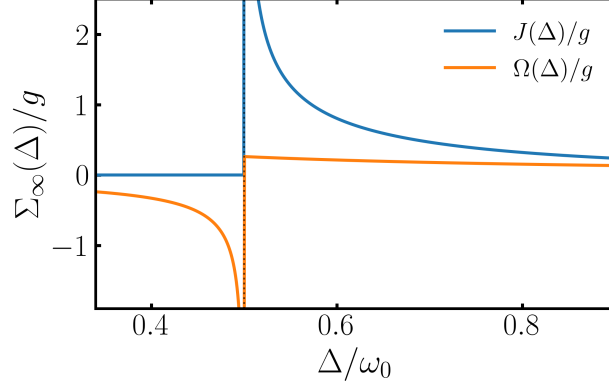


FIG. S2. **Self-energy function.** Lamb's shift $\Omega(\Delta) = \Re\Sigma_\infty(\Delta)$ and spectral function $J(\Delta) = -2\Im\Sigma(\Delta)$ for infinite UV cutoff. The vertical dotted line at $\Delta = \omega_0/2$ marks the lower-band edge in LHTL, where both $\Omega(\Delta)$ and $J(\Delta)$ diverge.

For infinite cutoff $\omega_c \rightarrow \infty$,

$$\begin{aligned} \Sigma_\infty(E) &= \frac{g^2}{2\pi} \int_{-\pi}^{\pi} \frac{dk}{E - \omega_0/2 |\sin(k/2)|} \\ &= \begin{cases} \frac{g^2}{E} \left[1 + \frac{4\omega_0}{\pi\sqrt{\omega_0^2 - 4E^2}} \tan^{-1} \left(\sqrt{\frac{\omega_0 + 2E}{\omega_0 - 2E}} \right) \right]; & E < \omega_0/2 \\ \frac{g^2}{E} \left[1 + \frac{2\omega_0}{\pi\sqrt{4E^2 - \omega_0^2}} \left\{ \ln \left(\frac{2E + \sqrt{4E^2 - \omega_0^2}}{\omega_0} \right) - i\pi \right\} \right], & E > \omega_0/2 \end{cases} \end{aligned} \quad (\text{S49})$$

In general the self-energy of a system is complex-valued and its real and imaginary parts correspond to frequency shift and decay of the qubit, see Fig. S2. More precisely, the retarded self-energy is written as,

$$\Sigma_\infty^R(E + i0^+) = \Omega(E) - \frac{iJ(E)}{2} \quad (\text{S50})$$

where $\Omega(E) = \Re(\Sigma_\infty^R(E + i0^+))$ is the Lamb's shift, and $J(E) = -2\Im(\Sigma_\infty^R(E + i0^+))$ is the spectral function corresponding to the effective decay rate of qubit into the waveguide.

S3. ALGEBRAIC BOUND-STATE ENVELOPE

The bound state can be written as,

$$|\psi_{\text{bound}}\rangle = C_e \left(\sigma^+ + \sum_k \frac{g_k^*}{E_{\text{bound}} - \omega_k} a_k^\dagger \right) |g, \mathbf{0}\rangle \quad (\text{S51})$$

where C_e is the bound-state normalization constant. We can expand the k -mode operator in terms of real space operators as,

$$\begin{aligned} |\psi_{\text{bound}}\rangle &= C_e \left(\sigma^+ + \sum_k \frac{g_k^*}{E_{\text{bound}} - \omega_k} \frac{1}{\sqrt{N}} \sum_n e^{-ikn} a_n^\dagger \right) |g, \mathbf{0}\rangle \\ &= C_e \left(\sigma^+ + \sum_n \underbrace{\frac{g}{N} \sum_k \frac{e^{-ik(n-m)}}{E_{\text{bound}} - \omega_k}}_{\phi_{n-m}} a_n^\dagger \right) |g, \mathbf{0}\rangle \end{aligned} \quad (\text{S52})$$

The bound-state profile around $m = 0$ site for LHTL is given as the average photon number at site n ,

$$\begin{aligned} \langle \Psi_{\text{bound}} | a_n^\dagger a_n | \Psi_{\text{BS}} \rangle &= |C_e|^2 \langle g, \mathbf{0} | \left(\sigma^- + \sum_j \phi_j^* a_j \right) a_n^\dagger a_n \left(\sigma^+ + \sum_k \phi_k a_k^\dagger \right) | g, \mathbf{0} \rangle \\ \langle a_n^\dagger a_n \rangle &= |C_e \phi_n|^2 \\ &= |C_e|^2 \left| \frac{g^2}{2\pi} \int_{-\pi}^{\pi} dk \frac{e^{-ikn}}{E_{\text{bound}} - \omega(k)} \right|^2 \end{aligned} \quad (\text{S53})$$

For $n \gg 1$, the integrand is stationary only around smallest $k \approx 0$. For large k , the integrand oscillates rapidly and integrating over any interval vanishes. The later argument also allows us to extend the integration limits to \mathbb{R} . Thus we expand the LHTL dispersion $\omega(k \approx 0) \approx \omega_0 n_* / \sqrt{1 + (n_* k)^2}$, and since usually $E_{\text{bound}} \ll \omega(k \approx 0)$, we approximate,

$$\frac{1}{E_{\text{bound}} - \omega(k \approx 0)} = -\frac{1}{\omega(k \approx 0)} \left(\frac{1}{1 - \frac{E_{\text{bound}}}{\omega(k \approx 0)}} \right) \simeq -\frac{1}{\omega(k \approx 0)}. \quad (\text{S54})$$

After these approximations, the integral in Eq. S53 is given as,

$$\langle a_n^\dagger a_n \rangle = \frac{g^2 |C_e|^2}{\omega_0^2 n_*^2} \left| \frac{1}{2\pi} \int_{-\infty}^{\infty} dk e^{-ikn} \sqrt{1 + (n_* k)^2} \right|^2, \quad (\text{S55})$$

which is the Fourier transform of $\sqrt{1 + (n_* k)^2}$ given as $-\frac{K_1(n/n_*)}{n\pi}$. This gives the closed form of the photon profile as,

$$\langle a_n^\dagger a_n \rangle \simeq \frac{g^2 |C_e|^2}{\pi^2 \omega_0^2 n_*^2} \left(\frac{K_1(n/n_*)}{n} \right)^2. \quad (\text{S56})$$

where $K_1(z)$ is the modified Bessel function of second kind of first-order. This analytical result is consistent with the numerics (single-excitation diagonalization) and remains surprisingly accurate even for relatively small n . The normalization constant $|C_e|^2$ is evaluated by demanding a normalized bound-state,

$$\begin{aligned} \langle \psi_{\text{bound}} | \psi_{\text{bound}} \rangle &= |C_e|^2 \langle g, 0 | \left(\sigma^- + \sum_k \frac{g_k}{E_{\text{bound}} - \omega_k} a_k \right) \left(\sigma^+ + \sum_k \frac{g_k^*}{E_{\text{bound}} - \omega_k} a_k^\dagger \right) | g, 0 \rangle \\ &= |C_e|^2 \left(\langle g, 0 | \sigma^- \sigma^+ | g, 0 \rangle + \sum_k \langle g, 0 | \frac{g_k^* \sigma^- a_k^\dagger + g_k \sigma^+ a_k}{E_{\text{bound}} - \omega_k} | g, 0 \rangle \right. \\ &\quad \left. + \sum_{k, k'} \frac{g_k g_{k'}^* \langle g, 0 | a_k a_{k'}^\dagger | g, 0 \rangle}{(E_{\text{bound}} - \omega_k)(E_{\text{bound}} - \omega_{k'})} \right) \\ &= |C_e|^2 \left(1 + \sum_k \frac{|g_k|^2}{(E_{\text{bound}} - \omega_k)^2} \right) \end{aligned} \quad (\text{S57})$$

Equating to unity, we obtain,

$$|C_e|^{-2} = 1 + \sum_k \frac{|g_k|^2}{(E_{\text{bound}} - \omega_k)^2}$$

But since, $\Sigma(E) = \sum_k \frac{|g_k|^2}{E - \omega_k}$, then

$$\frac{d\Sigma(E)}{dE} = -\sum_k \frac{|g_k|^2}{(E - \omega_k)^2} \quad (\text{S58})$$

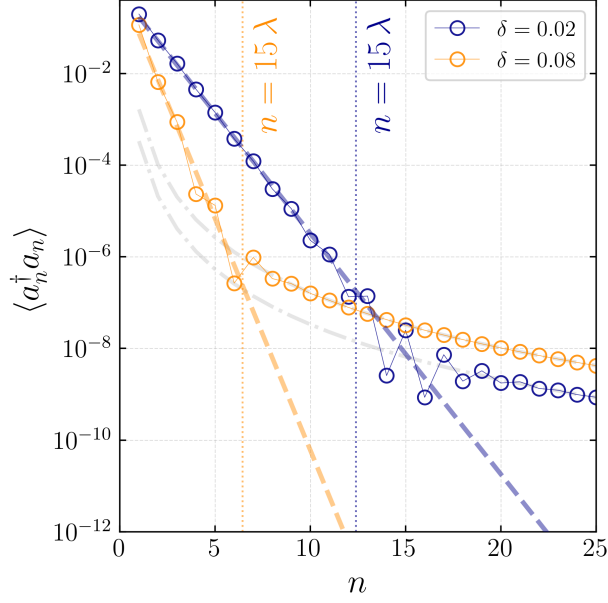


FIG. S3. **LHTL bound-state core exponential window.** Colored dashed lines show core exponential profile for two detunings $\delta = \omega_{\text{IR}} - E_{\text{bound}}$. The vertical dotted line marks an approximate exponential core extent. The gray dash-dot curve indicates the asymptotic algebraic decay ($1/n^4$) dominating at large distances, $n \gg \lambda$. Here $\omega_0 = 1$, $g/\omega_0 = 0.2$, $\omega_c \rightarrow \infty$.

thus we can write the normalization as,

$$|C_e| = \left[1 - \left. \frac{d\Sigma(E)}{dE} \right|_{E_{\text{bound}}} \right]^{-1/2} \quad (\text{S59})$$

A similar bound-state calculation can be done for RHTL starting from Eq. S53. Since the RHTL dispersion given by,

$$\omega_k^{\text{RH}} = \omega_c \sqrt{\frac{1 - \cos(k)}{\frac{\omega_c^2}{2\omega_0^2} + 1 - \cos(k)}} \quad (\text{S60})$$

is gapless, the emitter is parked above the band. In this case, $E_{\text{bound}} \gg \omega(k \approx 0)$, we approximate the integrand as,

$$\frac{1}{E_{\text{bound}} - \omega(k \approx 0)} = \frac{1}{E_{\text{bound}}} \left(\frac{1}{1 - \frac{\omega(k \approx 0)}{E_{\text{bound}}}} \right) \simeq \frac{1}{E_{\text{bound}}} + \frac{\omega(k \approx 0)}{E_{\text{bound}}^2}, \quad (\text{S61})$$

and the bound-state integral reads,

$$\langle a_n^\dagger a_n \rangle = \frac{\omega_0^2 g^2 |C_e|^2}{E_{\text{bound}}^4} \left| \frac{1}{2\pi} \int_{-\infty}^{\infty} dk e^{-ikn} |k| \right|^2 = \frac{\omega_0^2 g^2 |C_e|^2}{\pi^2 E_{\text{bound}}^4} \left(\frac{1}{n^4} \right), \quad (\text{S62})$$

S4. BOUND-STATE CORE: WAVEGUIDE QED NEAR THE BAND-EDGE

For the LHTL, when the qubit is parked just below the lower band edge, we define $\delta \equiv \omega_{\text{IR}} - E_{\text{bound}}$, besides the algebraic-exponential crossover set by n_* , there is a short-distance exponential core controlled by the quadratic expansion of the dispersion around $k \simeq \pi$. For simplicity, we work in the infinite cutoff limit.

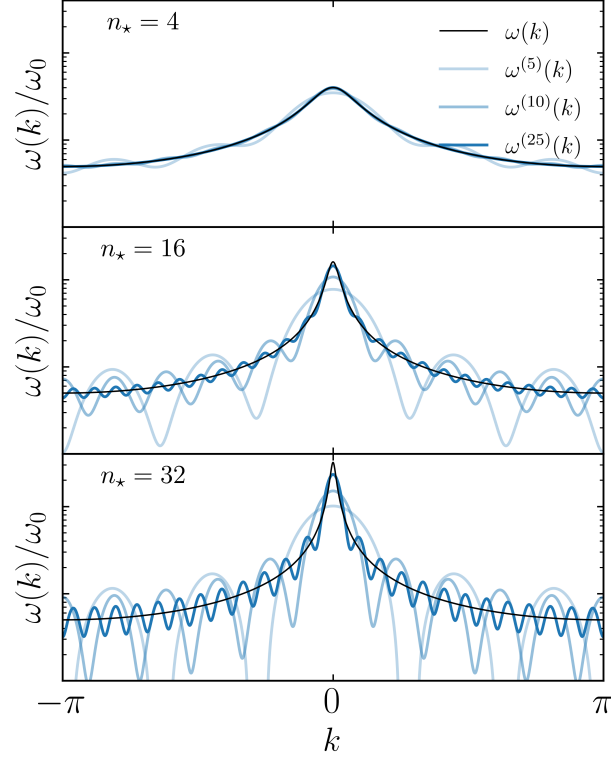


FIG. S4. **Dispersion relation.** Solid blue lines represent the dispersion relations obtained using Eq. S66 for $D = 5, 10, 25$. Black solid denotes the exact dispersion.

Writing $q = \pi - k$ and $\omega(k) \simeq (\omega_0/2)(1 + q^2/2)$, the bound-state kernel reduces to $(E_{\text{bound}} - \omega(k))^{-1} \simeq [\delta + (\omega_0/16)q^2]^{-1}$. Note that the approximation $E_{\text{bound}} - \omega(k) \approx -\omega(k)$ used in the previous section does not apply for these very short-distance fields. Evaluating the Fourier integral then gives, for separations $|n| \gtrsim 1$,

$$\langle a_n^\dagger a_n \rangle_{\text{LH}} \approx \frac{4g^2 |C_e|^2}{\omega_0 \delta} e^{-n/\lambda_{\text{LH}}}, \quad \lambda_{\text{LH}} \equiv \frac{1}{8} \sqrt{\frac{\omega_0}{\delta}}. \quad (\text{S5})$$

This corresponds to an intensity profile with a core localization length λ_{LH} . The near-field exponential is confined to $n \lesssim \text{few } \lambda_{\text{LH}}$, see Fig. S3. In the natural regime $\delta \gg \omega_0/64$ one has $\lambda_{\text{LH}} \ll 1$, so the short-distance exponential region is essentially restricted to the nearest unit cell.

A similar calculation for a qubit coupled to an RHTL yields

$$\langle a_n^\dagger a_n \rangle_{\text{RH}} \approx \frac{g^2 |C_e|^2}{\omega_0 \delta} e^{-n/\lambda_{\text{RH}}}, \quad \lambda_{\text{RH}} \equiv \frac{1}{4} \sqrt{\frac{\omega_0}{\delta}}. \quad (\text{S63})$$

In both cases the core length scales as $\lambda \propto \delta^{-1/2}$. Finite cutoffs in both lines only slightly modifies the localization length as long as $\omega_c > \omega_0$ —“good” waveguide regime.

S5. REPRODUCING THE DISPERSION BY EXTENDED HOPPING: LH TL AND RH TL

The mapped real-space photonic network in LH TL is defined as,

$$H_{\text{LH}} = \sum_{m \in \mathbb{Z}} \sum_{n \in \mathbb{Z}} \xi_n a_{m+n}^\dagger a_m + \text{h.c.},$$

$$\xi_n = \frac{1}{\pi} \int_0^\pi \omega(k) \cos(nk) dk$$
(S64)

Consider a spatially truncated Hamiltonian $H^{(D)}$ that only contains the nearest D -neighbor hopping,

$$H_{\text{LH}}^{(D)} = \sum_{m \in \mathbb{Z}} \sum_{n=-D}^D \xi_n a_{m+n}^\dagger a_m$$
(S65)

The dispersion relation for the truncated Hamiltonian $H^{(D)}$ is given as,

$$\omega^{(D)}(k) = \xi_0 + 2 \sum_{n=1}^D \xi_n \cos(kn)$$
(S66)

As shown in Fig. S4, the truncated $H^{(D)}$ fails to reproduce the dispersion unless $D \gg n_*$.

S6. EXACT DYNAMICS: INVERSE LAPLACE INTEGRATION

We mostly follow the techniques outlined in [1]. Continuing from the equation in the main text,

$$\dot{\tilde{C}}_e(t) = - \int_0^t K(\tau) \tilde{C}_e(t - \tau) d\tau,$$
(S67)

where $K(\tau) = \int_0^\infty \frac{d\omega}{2\pi} J(\omega) e^{-i(\omega - \Delta)\tau}$, we take the Laplace transform of Eq. S67,

$$\tilde{C}_e(s) = \frac{1}{s + K(s)},$$
(S68)

where $\tilde{C}_e(s) = L(\tilde{C}_e(t); s)$, $K(s) = L(K(t); s)$, and $L(f(t); s) = \int_0^\infty e^{-st} f(t) dt$ represent Laplace transform of $f(t)$. $K(s)$ can be evaluated as,

$$K(s) = \int_0^\infty \frac{d\omega}{2\pi} J(\omega) \frac{1}{s + i(\omega - \Delta)} = i \Sigma(is + \Delta),$$

where $\Sigma(z) = \int_0^\infty d\omega J(\omega)/(z - \omega)$ is the self-energy function. Finally, evaluating the inverse Laplace transform of $\tilde{C}_e(s) = [s + i \Sigma(is + \Delta)]^{-1}$ gives the qubit dynamics,

$$C_e(t) = \frac{1}{2\pi i} \int_{\sigma - i\infty}^{\sigma + i\infty} \frac{e^{\tilde{s}t} d\tilde{s}}{\tilde{s} + i\Delta + G(\tilde{s})}$$
(S69)

where $G(\tilde{s}) = i \Sigma(i\tilde{s})$, and $\tilde{s} = s - i\Delta$. The integrand has a branch cut at $\tilde{s} \in [-i\omega_0/2, -i\infty]$, hence we deform the contour such that it avoids crossing it, see Fig. 4A in the main text. This contour then contains a pole at $\tilde{s} = iy_p$, where y_p solves $y - \Delta - \Sigma(-y) = 0$. Evaluating this integral we get two terms, one from the discontinuity of self-energy near the branch cut (scattering term) and the other from the residue term (bound-state term),

$$C_e(t) = C_e^{(s)}(t) + C_e^{(b)}(t) = \frac{8g^2}{\pi\omega_0^2} \int_{-\infty}^{-1} dx M(x) e^{i\omega_0 x t/2} + r e^{iy_p t}$$
(S70)

where the spectral weight function $M(x)$ is given as,

$$M(x) = \frac{-x\sqrt{x^2-1}}{x^2(x^2-1) \left[x + \frac{2\Delta}{\omega_0} - \frac{4g^2}{\omega_0^2 x} \left(1 + \frac{2 \ln(\sqrt{x^2-1}-x)}{\pi\sqrt{x^2-1}} \right) \right]^2 + (2\sqrt{2}g/\omega_0)^4}, \quad (\text{S71})$$

$x \equiv 2y/\omega_0$ is a dimensionless energy parameter, and $r = [1 + G'(\tilde{s})]_{\tilde{s}=iy_p}^{-1}$ is the Cauchy residue and $G'(z) \equiv dG/dz$.

Exponential decay—For early times, the qubit decays into the spectrally closest modes available in the LHTL spectrum around which the weighting function $M(x)$ is approximately a Lorentzian. Thus, the major peak around the qubit frequency dictates its dynamics. Let the pole location in the complex-plane (which is same as peak location in real-space with a width corresponding to the imaginary part of pole location) be $x_0 \in \mathbb{C}$, therefore the denominator $D(x_0) = 0$, and $D'(x_0) \neq 0$, hence we approximate $M(x)$ around $x = x_0$ as,

$$\begin{aligned} M(x) &= \frac{N(x)}{D(x)} = \frac{N(x_0)}{D(x_0) + D'(x_0)(x-x_0) + D''(x_0)(x-x_0)^2/2 + \dots} \\ &\approx \frac{N(x_0)/D'(x_0)}{(x-x_0)} + \frac{N(x_0^*)/D'(x_0^*)}{(x-x_0^*)} \\ &= \frac{a_0}{x-x_0} + \frac{a_0^*}{x-x_0^*}, \quad a_0 \equiv \frac{N(x_0)}{D'(x_0)} \end{aligned} \quad (\text{S72})$$

The complex pole x_0 come in conjugate pairs and are calculated numerically by solving the following equation.

$$x_0^2(x_0^2-1) \left[x_0 + \frac{2\Delta}{\omega_0} - \frac{4g^2}{\omega_0^2 x_0} \left(1 + \frac{2 \ln(\sqrt{x_0^2-1}-x_0)}{\pi\sqrt{x_0^2-1}} \right) \right]^2 + (2\sqrt{2}g/\omega_0)^4 = 0 \quad (\text{S73})$$

To evaluate the qubit dynamics $C_e(t)$, we can safely extend the limits from $-\infty$ to $+\infty$ and using the residue theorem get,

$$\begin{aligned} C_e^{(s)}(t) &\approx -\frac{8g^2 a_0}{\pi\omega_0^2} \int_{-\infty}^{+\infty} dx \frac{e^{i\omega_0 x t/2}}{x-x_0} = -\frac{16ig^2 a_0}{\omega_0^2} e^{i\omega_0 x_0 t/2} \\ &= -\frac{16ig^2 a_0}{\omega_0^2} e^{-\gamma t/2} e^{i\delta t} \end{aligned} \quad (\text{S74})$$

where, $\gamma = \omega_0 \Im(x_0)$, and $\delta = \Re(x_0)\omega_0/2$. Note that only the pole in the upper-half of the complex plane contribute to the integral since the contour is chosen to close from above, so that γ is always positive. The population dynamics then reads,

$$|C_e^{(s)}(t)|^2 \approx \left(\frac{16g^2 |a_0|}{\omega_0^2} \right)^2 e^{-\gamma t} \quad (\text{S75})$$

Polynomial t^{-3} tail—At long times $t \gg 1/\gamma$, the most significant contribution to the dynamics comes from the band-edge near $x = -1$. Hence, we approximate the $M(x)$ around $x = -1$,

$$M_1(x) \approx \frac{1}{32\sqrt{2}} \left(\frac{\omega_0}{g} \right)^4 \sqrt{-1-x}, \quad x < -1 \quad (\text{S76})$$

Since the original weighting function vanishes for $x \rightarrow -\infty$, which is a requirement for the $C_e(t)$ integral to converge, we add a soft cut by introducing exponentially decaying factor to the approximation such that it does not affect the value of the function at $x = -1$.

$$\tilde{M}(x) \equiv e^{x+1} M_1(x) = \frac{1}{32\sqrt{2}} \left(\frac{\omega_0}{g} \right)^4 e^{x+1} \sqrt{-1-x} \quad (\text{S77})$$

The qubit dynamics $C_e(t)$ is then,

$$\begin{aligned} C_e^{(s)}(t) &\approx -\frac{8g^2}{\pi\omega_0^2} \frac{1}{32\sqrt{2}} \left(\frac{\omega_0}{g}\right)^4 \int_{-\infty}^{-1} dx e^{i\omega_0 x t/2} e^{x+1} \sqrt{-1-x} \\ &= -\frac{\omega_0^2}{8\sqrt{2}\pi g^2} \frac{e^{-i\omega_0 t/2}}{(1+i\omega_0 t/2)^{3/2}} \end{aligned} \quad (\text{S78})$$

Then the population dynamics read as,

$$|C_e^{(s)}(t)|^2 \simeq \frac{1}{16\pi} \left(\frac{\omega_0}{g}\right)^4 \frac{1}{(\omega_0 t)^3}, \quad \omega_0 t \gg 1 \quad (\text{S79})$$

S7. NUMERICAL DIAGONALIZATION FOR BOUND-STATE

To validate the continuum analysis, we also compute the qubit-photon bound-state profile by exact diagonalization of the single-excitation Hamiltonian for a finite waveguide with N modes. The Hamiltonian we diagonalize is,

$$H = \Delta \sigma^+ \sigma^- + \sum_k \omega_k a_k^\dagger a_k + \sum_k (g_k \sigma^+ a_k + g_k^* a_k^\dagger \sigma^-), \quad (\text{S80})$$

where Δ is the bare qubit frequency, ω_k is the dispersion relation of the transmission line, and g_k is the momentum-dependent coupling we derived in earlier sections. In the single-excitation sector we introduce the operator vector $\Phi = (\sigma^-, a_{k_1}, a_{k_2}, \dots, a_{k_N})^T$, so that the Hamiltonian can be compactly written as $H = \Phi^\dagger h(k) \Phi$, where

$$h(k) = \begin{pmatrix} \Delta & g_{k_1}^* & g_{k_2} & \cdots & g_{k_N} \\ g_{k_1}^* & \omega_{k_1} & 0 & \cdots & 0 \\ g_{k_2}^* & 0 & \omega_{k_2} & \cdots & 0 \\ \vdots & \vdots & \vdots & \ddots & \vdots \\ g_{k_N}^* & 0 & \cdots & \cdots & \omega_{k_N} \end{pmatrix} \quad (\text{S81})$$

The k -space Hamiltonian $h(k)$ is then diagonalized numerically to get $N + 1$ eigenvalues E_ν and their corresponding eigenvectors,

$$|\psi_{(\nu)}\rangle = C_e^{(\nu)} |e, 0\rangle + \sum_k C_k^{(\nu)} |g, 1_k\rangle \quad (\text{S82})$$

The bound states are identified by their eigenvalues E_ν lying outside the range $[\omega_{\text{IR}}, \omega_{\text{UV}}]$. For each of those eigenvalues, the photonic coefficients $C_k^{(\nu)}$ are stored and the real-space bound-state profile amplitudes are given as $\phi_n^{(\nu)} \equiv \langle g, 1_n | \psi_{(\nu)} \rangle$, where $\langle g, 1_n | = \langle g, 0 | a_n$ and $a_n^\dagger = N^{-1} \sum_k e^{-ikn} a_k^\dagger$, therefore is given as discrete Fourier transform,

$$\phi_n^{(\nu)} = \frac{1}{\sqrt{N}} \sum_k e^{ikn} C_k^{(\nu)}. \quad (\text{S83})$$

S8. NUMERICAL DIAGONALIZATION FOR DYNAMICS

To get the dynamics, we evolve the initial state $|\psi(0)\rangle = (1, 0, 0, \dots)^T$ by the unitary operator $U = e^{-iHt}$ as $|\psi(t)\rangle = e^{-iHt} |\psi(0)\rangle$. The Hamiltonian is diagonalized numerically to obtain the eigenvalues E_ν and the unitary eigenvector matrix V such that, $V^\dagger H V = \text{diag}(E_0, E_1, \dots, E_N) \equiv E$. Hence, any eigenstate $|E_j\rangle$ can be written as,

$$|E_j\rangle = \sum_{m=0}^N V_{mj} |m\rangle, \quad (\text{S84})$$

where $|0\rangle = |e, 0\rangle = |\psi(0)\rangle$, and $|k\rangle = |g, 1_k\rangle$. The evolution is then given as,

$$|\psi(t)\rangle = e^{-iHt}|\psi(0)\rangle = V e^{-iEt} V^\dagger |\psi(0)\rangle, \quad (\text{S85})$$

that can be projected onto the original basis as,

$$\psi_m(t) = \langle m|\psi(t)\rangle = \sum_{j=0}^N V_{mj} V_{0j}^* e^{-iE_j t}. \quad (\text{S86})$$

The qubit and photonic amplitudes are the first, and the remaining components of the vector $\psi_m(t)$, respectively.

$$C_e(t) \equiv \psi_0(t) = \sum_{j=0}^N |V_{0j}|^2 e^{-iE_j t}, \quad C_k(t) \equiv \psi_k(t) = \sum_{j=0}^N V_{kj} V_{0j}^* e^{-iE_j t}. \quad (\text{S87})$$

The photon real-space propagation, can be evaluated by the Fourier transform of $C_k(t)$ as

$$\phi_n(t) = \frac{1}{\sqrt{N}} \sum_k e^{ikn} C_k(t) \quad (\text{S88})$$

S9. LIGHT-CONE EXPRESSION

To quantify the spreading of an initially localized excitation, we extract an ϵ -light-cone from the site-resolved photon population. Concretely, for each site n we define an arrival time $t_\epsilon(n)$ as the earliest time at which the local signal exceeds a fixed threshold ϵ (with the same ϵ used for all n). We then introduce the dimensionless distance variable $z \equiv n/n_*$, and work with the arrival-time function $t_\epsilon(z) \equiv t_\epsilon(n = zn_*)$. For short-times, the photon dynamics follow,

$$t_\epsilon(z) = \frac{\epsilon}{\sqrt{\xi(z)}} \quad (\text{S89})$$

Following the running-exponent construction used in the main text, we parametrize the ϵ -cone by a *position-dependent* light-cone exponent $\gamma(z)$ via the integrated form

$$t_\epsilon(z) = t_\epsilon(z_0) \left(\frac{z}{z_0} \right)^{-\bar{\gamma}(z; z_0)}, \quad \bar{\gamma}(z; z_0) = \frac{1}{\ln(z/z_0)} \int_{z_0}^z \frac{\gamma(z')}{z'} dz'. \quad (\text{S90})$$

From Eq. S89, we get a simple relation between local light-cone exponent $\gamma(z) \equiv d \ln t(z)/d \ln z$, and local hopping exponent $\alpha(z)$,

$$\gamma(z) = \frac{\alpha(z)}{2} \quad (\text{short-time regime}), \quad (\text{S91})$$

hence also, $\bar{\gamma}(z; z_0) = \bar{\alpha}(z; z_0)/2$. To follow an ϵ -cone, taking $t_\epsilon(z_0)$ directly from the numerical simulation, where $z_0 = 1/n_*$.

For the LH TL, the running-exponent analysis yields

$$\gamma^{\text{LH}}(z) = z \frac{K_{3/4}(z)}{K_{1/4}(z)}, \quad (\text{S92})$$

which increases with z , crossing $\gamma = 1$ at $z = z_2 \approx 1.55$, where $\alpha(z_2) = 1$. As a result, $\gamma^{\text{LH}}(z) < 1$ for $z < z_2$ or equivalently $n < z_2 n_*$, implying accelerated fronts in this window, as shown in Fig. S5A–C. For $z > z_2$, the hopping network is short-range and we recover linear cones.

For RH TL, $\alpha^{\text{RH}}(z) = 2$, hence $\gamma^{\text{RH}} = 1$, giving linear cones at all distances, consistent with simulations in Fig. S5D–F.

[1] P. R. Berman, G. W. Ford, Spectrum in spontaneous emission: Beyond the Weisskopf-Wigner approximation. *Phys. Rev. A* **82**, 023818 (2010).

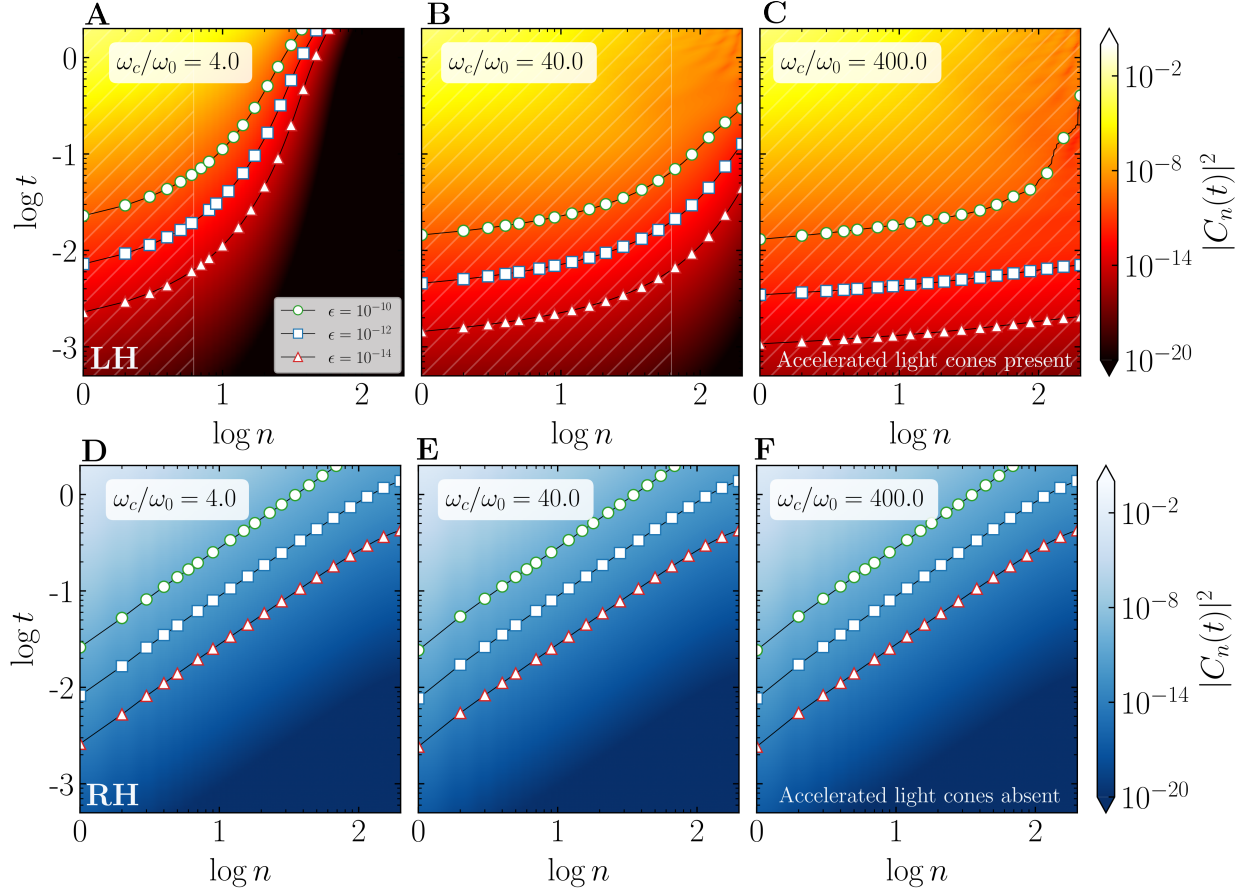


FIG. S5. **Light-cones in LHTL and RHTL.** Simulated photon intensity $|C_n(t)|^2$ along the transmission lines at different ω_c/ω_0 values, representing increasing n_* values ($N = 4001$, $\Delta/\omega_0 = 1$, $g/\omega_0 = 0.08$). The solid white markers, circle (10^{-10}), square (10^{-12}) and triangle (10^{-14}) denote different ϵ -cones, and the solid black lines are guides to the eye.